IEEE Transactions on Vehicular Technology, vol. 66, no. 11, pp. 9809-9824, Nov. 2017, doi: 10.1109/TVT.2017.2723729

Performance of Generalized Frequency Division Multiplexing Based Physical Layer in Vehicular Communications

Dan Zhang*, Andreas Festag†, and Gerhard Fettweis*

*Vodafone Chair Mobile Communication Systems, Technische Universität Dresden, Germany

{dan.zhang|gerhard.fettweis}@ifn.et.tu-dresden.de

†Fraunhofer Institute for Transportation and Infrastructure Systems (IVI), Dresden, Germany

andreas.festag@ivi.fraunhofer.de

***Abstract*—Vehicular communications enable information exchange among vehicles including the roadside infrastructure. This has led to applications to primarily increase road safety and traffic efficiency. Standardization efforts on vehicular communications are underway. The physical layer (PHY) is defined based on the IEEE 802.11 family of WiFi standards operating at the 5.9 GHz frequency band and on extensions of LTE; in both cases orthogonal frequency division multiplexing (OFDM) is the waveform of choice. Since the typical environment of WiFi deployment is very different to the vehicular communication environment, it is a challenging task to adapt the WiFi-based PHY for providing reliable and real-time communications under highly time- and frequency-selective fading channels. In this paper, the employment of an alternative waveform termed generalized frequency division multiplexing (GFDM) for vehicular communication is investigated. Specifically, a GFDM-based packet design is proposed on the basis of the standard-compliant OFDM-based PHY configuration. On the receiver side, this paper focuses on developing synchronization, channel estimation and equalization algorithms. The performance of the resulting GFDM-based PHY is verified and compared with the OFDM-based one by means of simulation. The obtained results demonstrate that the proposed GFDM-based PHY can utilize the time and frequency resources more efficiently, and outperform particularly under challenging channel conditions. Additionally, the low out-of-band (OOB) emission of GFDM is a desirable feature for future multi-channel operation (MCO) in vehicular communications.**

***Index Terms*—Intelligent transportation system (ITS), vehicular communications, OFDM, GFDM, inner receiver design**

I. Introduction

Vehicular communications are commonly regarded as a cornerstone of intelligent transportation systems (ITS). It increases the range of vision of vehicle sensors and improves the driver's awareness. The considered use cases include road safety and traffic efficiency, such as road hazard warning, road works warning, in-vehicle signage and green traffic light speed advisory. These use cases are mainly for driver's information and warning with moderate requirements on latency, reliability and throughput. In the future, vehicular communications can enable a very broad range of use cases. Among those, cooperative advanced cruise control (C-ACC), platooning, vulnerable road user (VRU) protection and urban ITS are currently being considered in research and standardization. Specifically, use cases related to communication support for vehicle automation rely on cooperative sensing and the exchange of maneuvering commands, which will have more stringent requirements on the wireless transmission.

The current standardized access technology for vehicular communications is based on a specific set of options of the IEEE 802.11 standard [1] operating at the 5.9 GHz frequency band allocated for safety and traffic efficiency in Europe and U.S, named ITS-G5 and WAVE, respectively [2], [3].[1] In addition to the IEEE 802.11-based solutions, enhancements of the cellular technology LTE for supporting vehicle-to-everything (V2X) communications are being specified by 3GPP (see e.g., [4]). Both, the IEEE 802.11-based solution and LTE-V2X, rely on orthogonal frequency division multiplexing (OFDM) as the waveform. Furthermore, for operation in the 5.9 GHz spectrum, both need to fulfill the regulatory requirements for RF output power, receiver selectivity and other parameters. Therefore, these requirements, e.g., defined in ETSI EN 302 571 for the European regulation, constitute the baseline for the minimum performance of the current generation of vehicular communications systems. Throughout this paper, we choose ITS-G5[2] to collectively name the access technology and use it as the baseline for our work on the physical layer (PHY) design for vehicular communication. However, the outcome of our investigation can be applied to other variants of vehicular communications systems.

In this paper, challenges on the PHY faced by vehicular communications systems are of concern. From extensive studies on channel modeling, e.g., in [5], [6], the vehicular communication channel can be highly selective in both time and frequency. Aiming at reliable data transmission under such a challenging scenario, ITS-G5 defines short OFDM symbols with long cyclic prefix (CP), accounting for 25% overhead in the usage of time resources.

The highly time- and frequency-selective vehicular commu-

[1] In the U.S., this set is referred to as wireless access in vehicular environment (WAVE), which was commonly known as the "p"-amendment to IEEE 802.11. The amendment was integrated into the IEEE 820.11-2012 and updated to the -2016 standard release. On the basis of WAVE, ITS-G5 is an European variant, adapting to European requirements.

[2] ETSI EN 302 663 and EN 302 571, URL http://etsi.org/standards

nication channel causes another challenge for the design of PHY: The receiver needs to track the fast time-varying channel for coherent detection. Analogous to IEEE 802.11a, ITS-G5 adopts a preamble for synchronization and channel estimation. However, channel estimation solely based on preamble is only suitable for relatively static channels, being initially targeted by IEEE 802.11a. For vehicular communication, the relative speed between two vehicles can be in the range of several hundred kilometers per hour. The initial preamble-based channel estimate will become outdated after a few OFDM data symbols. Even though each OFDM data symbol carries 4 pilot symbols, their spectral spacing is too large to yield accurate channel estimates for all active subcarriers. In fact, the original purpose of the 4 pilot symbols is to compensate the common phase error caused by the residual frequency offset (RFO) rather than to estimate the channel.

In the literature, the issue of fast time-varying vehicular communication channel has been studied intensively, see [7] for an overview. Briefly, two classes of solutions exist. The first modifies the frame structure of ITS-G5 by inserting additional training sequences, either at symbol [8]–[11] or at bit level [12] for data-aided (DA) channel estimation. However, additional training sequences will further reduce the temporal efficiency. The other class of solutions relies on decision-directed (DD) channel estimation. Namely, the data symbols fed back from the detector [13] or from the decoder [14] are treated as auxiliary pilot symbols for updating the channel estimates. The former one is subject to severe error propagation, since the symbol error rate at the output of detection is much higher than at the output of decoding. For the latter, the data symbols are subject to a processing latency caused by the decoder. However, this class of solutions does not require modification of the standard but comes at the cost of an increased receiver complexity and processing latency.

Last but not least, OFDM introduces large out-of-band (OOB) emission due to rectangular pulse shaping, which can yield high adjacent channel interference (ACI). The spectrum allocation in the $5.9\,$GHz frequency band assumes several $10\,$MHz channels including one primary safety channel, termed control channel (CCH), and other service channels (SCHs). Even though the planned initial deployment in Europe and U.S. considers only a single channel, it can be expected that with increasing equipment rate of vehicles and greater number of services, the other channels of the $5.9\,$GHz frequency band will also be exploited. In this case, ACI becomes a critical design issue for reliable and efficient communications. For multi-channel operation (MCO) two approaches exist: *(i)* A vehicle with a single-radio transceiver operates on one channel at a time and can periodically switch between CCH and any of the SCH. *(ii)* With dual-radio transceivers, one is permanently tuned to the CCH and the other can dynamically switch among SCHs. MCO is an active research area [15] and even though a first standard for MCO is available [16], the standardization process is still ongoing. In terms of spectrum emission masks associated to individual classes of devices [1], [17], the current allowable OOB emission is not low enough for simultaneous usage of the channels. Potential solutions to enable and to optimize MCO include transmit power reduction, restricted usage of channels adjacent to the CCH, synchronized transmission on adjacent channels and an improved spectrum emission mask [15].

From the above mentioned challenges, we come to the conclusion that OFDM may not be an efficient waveform for vehicular communication in terms of efficiency in the usage of time and frequency resources. To our knowledge, there has been no prior work in the literature that systematically and comprehensively investigates alternative waveforms in vehicular communications. In the field of mobile communications, the waveform study has been an important part of the ongoing research and development activities on the access technologies for the 5th generation (5G) communications systems [18], while OFDM is the 4th generation (4G) solution.

Major candidate waveforms for 5G systems, but not limited to them, include filtered OFDM [19], universal-filtered OFDM [20], filter bank multicarrier (FBMC) [21] and generalized frequency division multiplexing (GFDM) [22]. The first two waveforms apply linear filtering on the basis of OFDM to eliminate the interference between adjacent users. Naturally, this approach is usable for reducing ACI in the context of MCO as well. However, linear filtering also introduces additional interference between OFDM symbols. This can lead to severe performance degradation in highly frequency-selective channels. If the CP length increases for better protection, the temporal efficiency would be further decreased. Different to OFDM and its variants, both FBMC and GFDM are non-orthogonal waveforms. While suffering from self-generated interference, they also provide an additional degree of freedom in the time domain, namely, each subcarrier can carry multiple data symbols. The choice of filtering is an important design aspect of the non-orthogonal waveforms. FBMC applies linear filtering and achieves ultra-low OOB emission without being block-based. GFDM adopts circular filtering, which yields a block-based waveform with no filter tails and accomplishes a good compromise in the usage of both time and frequency resources. In this paper, we choose GFDM and focus on tailoring it for an improved PHY performance under challenging vehicular communication channels. We note that different variations of waveforms exist; for example the authors of [23] changed the linear filter in FBMC to circular. Therefore, the concepts proposed for GFDM in this paper may also be applicable to other block-based waveforms, but this is beyond the scope of this paper.

The main contribution of this work is summarized as follows. First, we derive a configuration of GFDM for vehicular communications based on ITS-G5. In particular, the technique termed unique word (UW), initially developed for discrete Fourier transform (DFT) spreading OFDM (DFT-s-OFDM) [24]–[27],[3] is applied on top of GFDM. Two novel and simple modifications are proposed to further reduce OOB emissions and relieve the negative impact of UW insertion on the data transmission. Using the UW as a training sequence, the second contribution on the GFDM receiver design involves algorithm development for UW based RFO and channel esti-

[3]Single-carrier frequency division multiple access (SC-FDMA) can be regarded as a special case of DFT-s-OFDM.

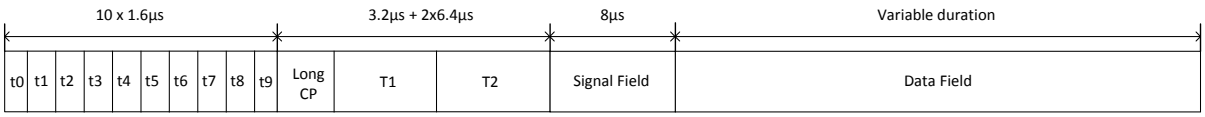

Fig. 1. Packet structure of ITS-G5 at the PHY.

mation. In particular, we derive a low complexity variant of sparse Bayesian learning (SBL) [28] for channel estimation. It is named factorized variational SBL (FV-SBL). Compared to the standard maximum-likelihood (ML) and linear minimum mean square error (LMMSE) criterion based channel estimation [29], our scheme is able to exploit the sparsity of the channel for an improved estimation quality without requiring prior knowledge of channel statistics. It is also usable for assisting fine synchronization. Since GFDM is a non-orthogonal waveform in general, a straightforward application of LMMSE equalization can cost much higher complexity than that of OFDM. Therefore, we aim at low complexity implementation that can support a high-level of parallelism in computation. Finally, we evaluate the performance achieved by GFDM in terms of transmit power spectral density (PSD), packet error rate (PER) and PHY-level throughput, while the performance attained with the standard-compliant OFDM setup is provided as a baseline.

The remainder of the paper is organized as follows: Section II gives a brief overview of the PHY configuration in ITS-G5. On this basis, a GFDM-based PHY design is proposed in Section III followed by the corresponding GFDM inner receiver design in Section IV. We evaluate its performance and compare it with the OFDM-based PHY in Section V. The whole paper is summarized and concluded by Section VI.

II. OFDM for Vehicular Communication

Fig. 1 depicts the packet structure at the PHY specified by ITS-G5. Each packet starts from a $32\,\mu$s preamble followed by a $8\,\mu$s signal and variable-length data fields. Specifically, the preamble consists of 10 identical short training symbol sequences, each of which lasts $1.6\,\mu$s. They are used for packet detection and coarse synchronization. The subsequent $3.2\,\mu$s long CP followed by two identical $6.4\,\mu$s long training symbol sequences are designed for fine synchronization and initial channel estimation. The signal field contains the rate and length information of the packet. The data field is comprised of a number of OFDM data symbols that adopt the configuration given in Table I and III.

The number N_{ofdm} of OFDM symbols per packet is determined by the ratio of the overall length of the packet and the number N_{bpofdm} of information bits per OFDM symbol

$$N_{\mathrm{ofdm}} = \left\lceil \frac{8N_{\mathrm{pl}} + 16 + 6}{N_{\mathrm{bpofdm}}} \right\rceil, \tag{1}$$

where $\lceil\cdot\rceil$ stands for the ceiling function. The overall length of packet is mainly determined by the payload size N_{pl} (in bytes) conveyed by the packet (more precisely the size of the PHY layer Service Data Units, PSDU). The additional 16 and 6 bits in the numerator of (1) denote the *service* and *tail* field in the PHY header and trailer as defined in [1], [30]. The number N_{bpofdm} of information bits per OFDM symbol in the denominator depends on the adopted OFDM configuration. Note that hereafter we refer N_{pl} to as the packet size.

TABLE I
ITS-G5 OFDM Configuration

Parameter	Value
Carrier frequency	5.9 GHz
Bandwidth[4]	10 MHz
(I)DFT size	64
Number of data subcarriers	48
Number of pilot subcarriers	4
Subcarrier spacing	156.25 kHz
CP duration	$1.6\,\mu$s
OFDM symbol duration	$6.4\,\mu$s
FEC	Convolutional code ($\{133, 171\}_8$)

Let us denote an OFDM symbol as $s[n]$

$$s[n] = \frac{1}{\sqrt{K}} \sum_{k=-K/2}^{K/2-1} d_k e^{j2\pi \frac{kn}{K}},\ n = 0, \ldots, K-1, \tag{2}$$

where K stands for the IDFT size and d_k can be data symbol, pilot symbol or zero, depending on the type of the subcarrier k, namely, data subcarrier, pilot subcarrier or inactive subcarrier. At the sampling rate 10 MHz, the $1.6\,\mu$s CP produces $L_{\mathrm{cp}} = 16$ samples, which is identical to the last L_{cp} samples of $s[n]$.

III. GFDM for Vehicular Communication

Starting from some basics of GFDM, this section presents a novel GFDM configuration for vehicular communication. Namely, we propose to combine GFDM with a UW signal in order to: *(i)* further reduce the OOB emission of GFDM, *(ii)* use the UW signal as a training sequence for RFO compensation and channel tracking, and (*iii*) avoid dedicated CP insertion.

A. Basics

Assume a GFDM symbol occupies K subcarriers, see Fig. 2. Each subcarrier can at most carry M data symbols, which are temporally equally spaced and circularly filtered by a pulse shaping filter $g(t)$. Denoting the temporal spacing as T, one period of $g(t)$ and the subcarrier spacing equal MT and $1/T$, respectively. At the sampling rate K/T, the discrete-time model of one GFDM symbol can then be written as

$$s[n] = \sum_{k=-K/2}^{K/2-1} \sum_{m=0}^{M-1} d_{k,m}\, g\left[\langle n - mK \rangle_N\right] e^{j2\pi \frac{k}{K} n},$$
$$n = 0, 1, \ldots, N-1, \tag{3}$$

[4]The sampling rate equals the bandwidth.

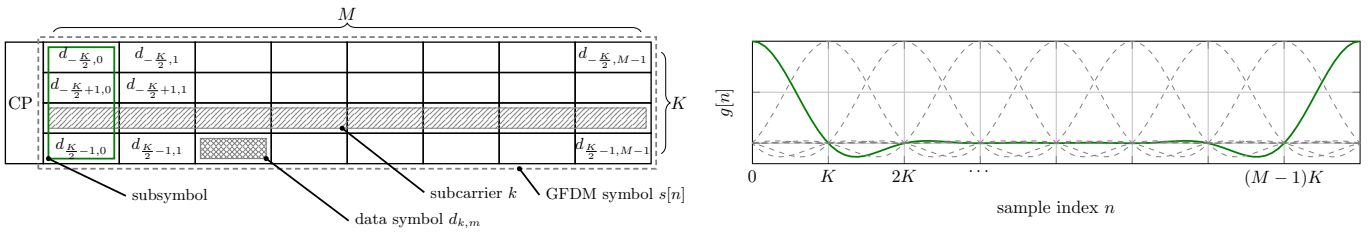

(a) GFDM time-frequency grid

(b) Circular pulse shaping

Fig. 2. Time-frequency grid of GFDM and terminology.

where $d_{k,m}$ stands for the symbol carried by the subcarrier k and transmitted at the time instant m, $g[n]$ equals $g(t = nT/K)$ for $n = 0, 1, \ldots, N-1$ with $N = MK$, i.e., one period, and $\langle a \rangle_b$ represents the operation a modulo b. Without loss of generality, here we normalize $\sum_{n=0}^{N-1} |g[n]|^2$ to one. If certain subcarriers of a subsymbol are inactive, this implies the corresponding symbols can only have the value zero. Compared to OFDM, the common configuration of GFDM also adopts CP to combat multipath fading, but uses a single one to protect M symbols on the same subcarrier, see Fig. 2.

B. Unique Word (UW) GFDM

The general goal of the UW schemes developed for DFT-s-OFDM is to have a fixed tail per DFT-s-OFDM symbol [24]–[27]. Analogously, the proposed UW design for GFDM also aims to ensure that each GFDM symbol has a fixed segment within the overall N samples but with two key differences: the location and the form of the fixed segment.

Due to circular filtering, a GFDM symbol is confined to the time interval $[0, MT]$. The tail biting effect creates disruptive changes on the boundaries, accounting for the major part of its OOB emission [22]. Fig. 2-(b) indicates that the head and tail of a GFDM symbol $s[n]$ are mainly influenced by the first subsymbol. To remove the disruptive changes, we aim at setting the first subsymbol in a way such that the first $L_{\rm hd}$ and last $L_{\rm tl}$ samples of $s[n]$ become data-independent, see Fig. 3. In other words, the head and tail of every GFDM symbol are fixed, while the head can be different to the tail.[5] If the length $L_{\rm tl}$ is greater than CP, the tail of the GFDM symbol i effectively serves as the CP for the GFDM symbol $(i+1)$ without inserting a dedicated CP as OFDM and the conventional GFDM do.

We note that the fixed head and tail will primarily and respectively affect the transmission of the second and last subsymbol. Targeting the same number $L_{\rm fix}$ of fixed samples per GFDM symbol, the approaches in the literature, which position all fixed samples at the tail ($L_{\rm hd} = 0$ and $L_{\rm tl} = L_{\rm fix}$), tend to severely deteriorate the transmission of the last subsymbol. This makes the last subsymbol much more vulnerable to channel impairments than the other subsymbols. A large number of burst errors can result in the loss of the whole packet. On the contrary, our approach ($L_{\rm hd} = L_{\rm tl} = L_{\rm fix}/2$) lets the second subsymbol equally share the negative impact with the last one, thereby reducing the number of burst errors.

Specifically, the determination of such first subsymbol resorts to a matrix-vector representation of linear GFDM modulation [22]. Let us concatenate the symbols carried by the active subcarriers of the first subsymbol into a vector $\mathbf{d}_0$. By analogy, we denote the rest symbols carried by the other $M-1$ subsymbols as $\mathbf{d}_{\setminus 0}$. On this basis, the N samples of $s[n]$ can be viewed as the entries of the vector $\mathbf{s}$ given as

$$\mathbf{s} = \mathbf{A}_0 \mathbf{d}_0 + \mathbf{A}_{\setminus 0} \mathbf{d}_{\setminus 0} + \mathbf{s}_{\rm uw}, \tag{4}$$

where $\mathbf{A}_0$ and $\mathbf{A}_{\setminus 0}$ are the modulation matrix with respect to the first and the rest $(M-1)$ subsymbols, and $\mathbf{s}_{\rm uw}$ denotes the UW signal embedded with the N GFDM samples.

The first subsymbol $\mathbf{d}_0$ is chosen to achieve

$$\begin{bmatrix} \mathbf{A}_{\rm hd,0} \\ \mathbf{A}_{\rm tl,0} \end{bmatrix} \cdot \mathbf{d}_0 + \begin{bmatrix} \mathbf{A}_{\rm hd,\setminus 0} \\ \mathbf{A}_{\rm tl,\setminus 0} \end{bmatrix} \cdot \mathbf{d}_{\setminus 0} = \mathbf{0}, \tag{5}$$

where the matrix $\mathbf{A}_{\rm hd,(\cdot)}$ and $\mathbf{A}_{\rm tl,(\cdot)}$ respectively take the first $L_{\rm hd}$ rows and the last $L_{\rm tl}$ rows of $\mathbf{A}_{(\cdot)}$. Since $\mathbf{d}_{\setminus 0}$ is known by the transmitter, we can compute $\mathbf{d}_0$ by solving the linear system given in (5)

$$\begin{aligned} \mathbf{d}_0 = &- \left[\mathbf{A}_{\rm hd,0}^H \mathbf{A}_{\rm hd,0} + \mathbf{A}_{\rm tl,0}^H \mathbf{A}_{\rm tl,0} + \gamma \mathbf{I}\right]^{-1} \\ &\cdot \left[\mathbf{A}_{\rm hd,0}^H \mathbf{A}_{\rm hd,\setminus 0} + \mathbf{A}_{\rm tl,0}^H \mathbf{A}_{\rm tl,\setminus 0}\right] \mathbf{d}_{\setminus 0}, \end{aligned} \tag{6}$$

where γ is parameter with a small enough value (e.g., 10^{-3}) to ensure an invertible matrix.

Due to (5), the first $L_{\rm hd}$ and last $L_{\rm tl}$ samples of $\mathbf{s}$ are determined by $\mathbf{s}_{\rm uw}$. In contrast to $\mathbf{d}_0$ and $\mathbf{d}_{\setminus 0}$, the vector $\mathbf{s}_{\rm uw}$ of length N is deterministic such that each GFDM symbol $\mathbf{s}$ has a fixed head and tail, which can be exploited by the receiver for fine synchronization and channel tracking. Here, we choose to generate $\mathbf{s}_{\rm uw}$ by means of GFDM modulation. Since only its first $L_{\rm hd}$ and last $L_{\rm tl}$ samples are of concern, only the first subsymbol needs to be activated, i.e., keep the terms with $m = 0$ in (3). As a result, the entry n of $\mathbf{s}_{\rm uw}$ equals

$$s_{\rm uw}[n] = \sum_k d_{k,0}^{\rm uw} g_{\rm uw}[n] e^{j2\pi \frac{kn}{K}}. \tag{7}$$

It is noted that the circular pulse shaping filter $g_{\rm uw}[n]$ adopted by the UW signal can be different to that used for data transmission. Regarding the choice of $\{d_{k,0}^{\rm uw}\}$, we use a Zadoff-Chu (ZC) sequence[6], considering its flat frequency-domain response and constant time-domain amplitude.

[5]Here, the length $L_{\rm hd}$ and $L_{\rm tl}$ shall be smaller than $K/2$. For larger values, it is not enough to just use the first subsymbol. However, the following presented steps can be straightforwardly extended for having an increased number of fixed samples by enabling more subsymbols for the UW signal.

[6]Here it is generated by calling the matlab function $\mathrm{lteZadoffChuSeq}(\cdot)$ with the 23th root.

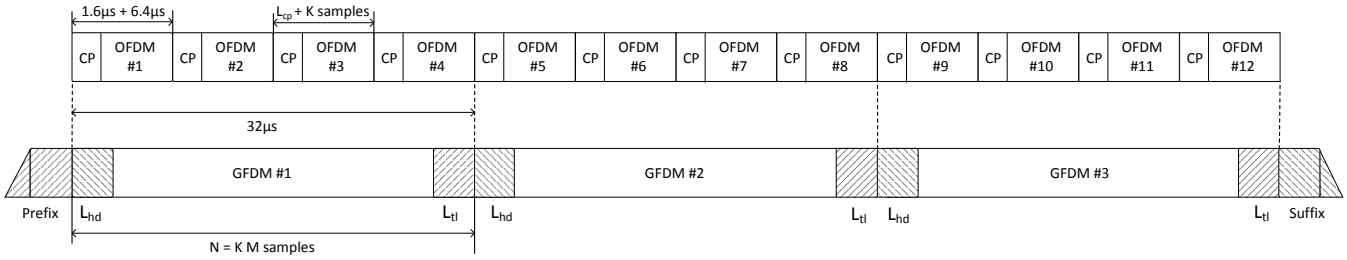

Fig. 3. Structure of the data field for the GFDM-based PHY compared with the OFDM based one.

TABLE II
UW-GFDM CONFIGURATION

Parameter	Value
Carrier frequency	5.9 GHz
Bandwidth	10 MHz
(I)DFT size	64
Subcarrier spacing	156.25 kHz
Number of subsymbols	5
GFDM symbol duration	32 μs
UW head and tail duration	2.4 μs
CP duration	0
Number of data subcarriers	52
Number of pilot subcarriers	0
Number of subcarriers used for the UW	57
Circular pulse shaping filter	periodic RC filter
Prefix of the first UW-GFDM symbol	6.3 μs
Suffix of the last UW-GFDM symbol	6.4 μs

For generating the above-described UW-GFDM, one direct way is to view (6) as an instance of precoding $\mathbf{d}_{\setminus 0}$, where the precoder is pre-calculable. After calculating $\mathbf{d}_0$, we feed it together with $\mathbf{d}_{\setminus 0}$ into the standard GFDM modulation unit [31] followed by adding the pre-defined UW signal (7).

C. Packet Design Using UW-GFDM

Using UW-GFDM, this subsection proposes a packet design based on ITS-G5 (see Fig. 3). The preamble and the signal field of the ITS-G5 packet structure in Fig. 1 are preserved, while we only replace UW-GFDM instead of OFDM for data transmission, see Table II.

Compared to the OFDM configuration in Table I, we first let UW-GFDM adopt the same DFT size and subcarrier spacing such that the sampling rate is identical. Each subsymbol has the same duration as one OFDM (without CP). Since each UW-GFDM symbol uses $M-1$ subsymbols (except the first one) for data transmission, the overhead is equivalent to the overall CP overhead of 4 OFDM symbols. In order to achieve an equal or a higher spectral efficiency than OFDM, the number M of subsymbols per UW-GFDM symbol should be no less than 5. Since a small M is preferred from the implementation perspective, here we adopt $M=5$ such that transmission of one UW-GFDM symbol lasts $32\,\mu$s, see Fig. 3.

Among the 5 subsymbols, we then use the first one to generate the UW signal such that the initial and last $2.4\,\mu$s of each GFDM symbol are nearly identical. In the configuration of OFDM, the CP with duration $1.6\,\mu$s is considered to be sufficient to combat multipath fading. This suggests that the $2.4\,\mu$s tail of the former UW-GFDM symbol is long enough to serve as the CP for the latter one without an extra guard time interval in between. The other 4 subsymbols are for data-carrying. Since the UW signal will be exploited for RFO compensation and channel estimation, the 4 pilot subcarriers with indices $\{\pm 21, \pm 7\}$ in ITS-G5 become re-usable for data transmission, leading to overall 52 data subcarriers with indices $\{\pm 26, \pm 25, \ldots, \pm 1\}$. For generating the UW signal, we let the first subsymbol additionally adopt the subcarriers with indices $\{0, \pm 27, \pm 28\}$ for assisting the receiver to achieve a good channel estimation quality on every data subcarrier. It is noted that the use of $\{\pm 27, \pm 28\}$ will widen the PSD of UW-GFDM. However, due to the low OOB emission of UW-GFDM, this design still fulfills the requirements in the standard, see Section V-A.

According to the configuration from above, we can calculate the number N_{bpgfdm} of information bits carried by one UW-GFDM symbol and then determine the number of UW-GFDM symbols for a given packet size N_{pl} analogous to (1)

$$N_{\mathrm{gfdm}} = \left\lceil \frac{8N_{\mathrm{pl}} + 16 + 6}{N_{\mathrm{bpgfdm}}} \right\rceil. \tag{8}$$

We note that one UW-GFDM symbol has the same duration as 4 OFDM symbols plus CPs. Since the 4 data-carrying subsymbols per UW-GFDM symbol adopt 4 more subcarriers than OFDM for data transmission, UW-GFDM yields ≈ 1.08 times higher data rate, see Table III.

Finally, we add a prefix to the first UW-GFDM symbol and a suffix to the last UW-GFDM symbol in the packet such that the transmission of the N_{gfdm} UW-GFDM symbols starts from and terminates to zero without disruptive changes in between to ensure low OOB emission. Considering the use of periodic raised cosine (RC) filters, the zero crossings of $g[n]$ and $g_{\mathrm{uw}}[n]$ are at the integer multiples of K, except $n=0$, e.g., in Fig. 2-(b). Therefore, the prefix and suffix are determined by the last $K-1$ and first K samples of (7), which last $6.3\,\mu$s and $6.4\,\mu$s, respectively. Since UW-GFDM achieves a higher data rate than OFDM, the overhead of the prefix and suffix can be compensated as long as each packet contains the information that needs at least 21 OFDM symbols to carry.

IV. GFDM RECEIVER ALGORITHMS

The task of the receiver is to recover the transmitted message based on the noisy channel observation. After successfully detecting the presence of a signal, the baseband processing at the receiver typically starts from synchronization. In this paper, we focus on estimating and compensating the

TABLE III
RATE DEPENDENT PARAMETER

MCS index	Code rate	Modulation scheme	Data rate [Mbps] (OFDM)	(GFDM)
1	1/2	BPSK	3	3.25
2	1/2	QPSK	6	6.5
3	1/2	16 QAM	12	13
4	2/3	64 QAM	24	26
5	3/4	BPSK	4.5	4.875
6	3/4	QPSK	9	9.75
7	3/4	16 QAM	18	19.5
8	3/4	64 QAM	27	29.25

dominant symbol-timing offset (STO) and carrier frequency offset (CFO). On this basis, channel estimation is further conducted for subsequent coherent equalization and detection.

Let us denote the sample sequence of the transmitted packet as $x[n]$. Its experienced time-varying multipath fading channel (in discrete-time model) has $L_{\rm ch}$ delay paths, where $L_{\rm ch}$ corresponds to the maximum channel delay length normalized by the sampling period. Considering the purpose of CP insertion, here we presume $L_{\rm ch} < L_{\rm cp}$. At the receiver, the received samples under STO ϵ and CFO Ω (normalized by the subcarrier spacing) are given as

$$r[n] = \left(\sum_{l=0}^{L_{\rm ch}-1} h_l[n-\epsilon] x[n-\epsilon-l] \right) e^{j2\pi \frac{\Omega n}{K}} + w[n], \quad (9)$$

where $w[n]$ is the additive white Gaussian noise (AWGN) with zero mean and variance N_0, and $h_l[n]$ represents the channel coefficient of the lth delay path at the time instant n. Here we note that it is a common practice to model the STO ϵ as an integer and let its fractional part be integrated with the channel impulse response (CIR).

A. Preamble-Based Synchronization

The initial task is synchronization based on the ITS-G5 preamble as depicted in Fig. 1. Specifically, we follow the approach in [32] to perform coarse STO and CFO estimation with appropriate modification. For further fine STO estimation, the authors of [32] relied on the ML estimate of CIR. Here, we propose to replace it by SBL [28], since the latter can exploit the sparsity of the CIR for an improved estimation quality. Considering the implementation constraint, we derive a low complexity SBL variant termed FV-SBL, see Appendix A.

1) Coarse STO Estimation: At the sampling rate 10 MHz, the initial 10 identical short training sequences in the preamble yields 160 samples with period 16. Given such repetitive structure, the timing metric is first calculated as [32]

$$\Lambda_\epsilon(\delta) = \left(\frac{10}{9} \frac{|P(\delta)|}{E(\delta)} \right)^2, \quad (10)$$

where the functions $P(\delta)$ and $E(\delta)$ are defined as

$$P(\delta) = \sum_{u=0}^{8} \sum_{v=0}^{15} r^*[\delta + 16u + v] r[\delta + 16(u+1) + v], \quad (11)$$

$$E(\delta) = \sum_{u=0}^{9} \sum_{v=0}^{15} |r[\delta + 16u + v]|^2. \quad (12)$$

Due to the channel dispersion, the maximum point $\delta_{\max}$ of $\Lambda_\epsilon(\delta)$ tends to be larger than the true STO ϵ. At the stage of coarse STO estimation, we subtract $\delta_{\max}$ by a time shift $\xi_{\rm c}$

$$\hat{\epsilon}_{\rm c} = \delta_{\max} - \xi_{\rm c} \quad (13)$$

and it shall be larger than the average time shift arising from channel dispersion. Without any prior knowledge of the channel, we set $\xi_{\rm c} = 8$, i.e., being identical to half CP length.

2) CFO Estimation: Using the coarse STO estimate $\hat{\epsilon}_{\rm c}$, we further extract the received samples $\{r_{\rm sht}[n]\}_{n=0,1,\ldots,143}$ in the sequence $r[n]$ that are supposedly associated to the last 9 short training sequences. Within such a short time interval, the CIR variation is unnoticeable. Therefore, apart from a multiplicative complex exponential due to CFO, the extracted 144 samples shall be repeated every 16 samples in a noise-free case.[7] Exploiting such repetitive structure, the CFO estimate is then computed as [32]

$$\hat{\Omega} = \frac{9}{2\pi} \sum_{u=1}^{5} w(u) \phi(u), \quad (14)$$

where $w(u)$ and $\phi(u)$ are given as

$$w(u) = \frac{(9-u)(9-u+1) - 20}{120} \quad (15)$$

$$R(u) = \frac{1}{144 - 16u} \sum_{n=16u}^{143} r^*_{\rm sht}[n-16u] r_{\rm sht}[n] \quad (16)$$

$$\phi(u) = \left[\arg R(u) - \arg R(u-1) \right]_{2\pi}. \quad (17)$$

In above, $\arg R(u)$ takes the argument of $R(u)$ and the modulo 2π operation $[a]_{2\pi}$ reduces a to the interval $[-\pi, \pi)$.

The CFO estimation range of this approach is ± 4.5 (normalized by the subcarrier spacing) [32]. As specified by the standard [1], the oscillator precision tolerance should be less than ± 20 ppm, implying the normalized CFO Ω is in the range from -1.51 to $+1.51$. Evidently, it is within the acquisition range of the above-presented approach, implying the RFO $\Omega_{\rm f} = \Omega - \hat{\Omega}_{\rm c}$ shall be relatively small. However, any non-zero RFO will still generate a non-negligible common phase offset on the data symbols [33], which needs to be properly compensated during the reception of each GFDM data symbol.

3) FV-SBL Assisted Fine STO Estimation: The two identical long training sequences in the preamble (see Fig. 1) are usable for channel and fine STO estimation. The long CP yields 32 samples, providing the robustness against the residual STO $\epsilon_{\rm f} = \epsilon - \hat{\epsilon}_{\rm c}$. With $0 \le \epsilon_{\rm f} \le 32 - L_{\rm ch}$, the residual STO only results in a cyclic shift in the received long training sequences, which can be further viewed as the outcome of cyclic convolution between the long training sequence $s_{\rm lng}[n]$ and a circularly shifted CIR plus noise. Since $\epsilon_{\rm f}$ determines the time shift in CIR, we can estimate it by tracking the delay of the first significative paths in the estimated CIR.

Specifically, given the coarse STO estimate $\hat{\epsilon}_{\rm c}$, the first received sample of the two long training sequences shall be $r[\hat{\epsilon}_{\rm c} + 192]$, where 192 is the number of received samples associated to the 10 short training sequences plus the long

[7] Each short training sequence, except the first one, can treat its former one as the CP for combating the multipath fading channel.

CP. After compensating the CFO based on $\hat{\Omega}$, the two received long training sequences can be conveniently expressed as

$$r_{\mathrm{lng}}^{[b]}[n] = e^{-j2\pi\frac{\hat{\Omega}(n+\hat{\epsilon}_{\mathrm{c}}+192+bK)}{K}} r[n+\hat{\epsilon}_{\mathrm{c}}+192+bK] \quad (18)$$

for $n = 0, 1, \ldots, K-1$, and b stands for the index of the two long training sequences with $b \in \{0, 1\}$. Based on (9), eq. (18) can be further expanded as

$$r_{\mathrm{lng}}^{[b]}[n] = \sum_{l=0}^{L_{\mathrm{ch}}-1} h_l[n+\hat{\epsilon}_{\mathrm{c}}+192+bK] e^{j2\pi\frac{\Omega_{\mathrm{f}}(n+bK)+\theta}{K}} \cdot s_{\mathrm{lng}}[\langle n-\epsilon_{\mathrm{f}}-l\rangle_K] + \tilde{w}_{\mathrm{lng}}^{[b]}[n], \quad (19)$$

where θ equal to $\Omega_{\mathrm{f}}(\hat{\epsilon}_{\mathrm{c}}+192)$ represents the cumulative effect of RFO from the past $\hat{\epsilon}_{\mathrm{c}}+192$ samples, and $\tilde{w}_{\mathrm{lng}}^{[b]}[n]$ is the Gaussian noise incorporating the CFO compensation. We can treat the exponential multiplicative term in (19) as a part of the CIR. The variation of such effective CIR during the short-time transmission of the two long training sequences is limited. Therefore, we can re-write (19) as

$$r_{\mathrm{lng}}^{[b]}[n] = \sum_{l=0}^{L_{\mathrm{ch}}-1} h_{\mathrm{avg},l}\, s_{\mathrm{lng}}[\langle n-\epsilon_{\mathrm{f}}-l\rangle_K] + I^{[b]}[n] + \tilde{w}_{\mathrm{lng}}^{[b]}[n] \quad (20)$$

with the average channel gain

$$h_{\mathrm{avg},l} = \frac{1}{2K}\sum_{n=0}^{2K-1} h_l[n+\hat{\epsilon}_{\mathrm{c}}+192] e^{j2\pi\frac{\Omega_{\mathrm{f}}n+\theta}{K}} \quad (21)$$

and a negligible interference $I^{[b]}[n]$ caused by the small change of the effective CIR [34]. Introducing K auxiliary variables $\{h'_{\mathrm{avg},l}\}_{l=0,\ldots,K-1}$ under the relation $h_{\mathrm{avg},l} = h'_{\mathrm{avg},\langle l+\epsilon_{\mathrm{f}}\rangle_K}$, a proper interchange of variables in (20) yields

$$r_{\mathrm{lng}}^{[b]}[n] = \sum_{l=0}^{K-1} h'_{\mathrm{avg},l}\, s_{\mathrm{lng}}[\langle n-l\rangle_K] + I^{[b]}[n] + \tilde{w}_{\mathrm{lng}}^{[b]}[n]. \quad (22)$$

Taking the average of the two observed training sequences and also treating the interference term as an additional noise, eq. (22) for $n = 0, 1, \ldots, K-1$ and $b \in \{0, 1\}$ can be compactly written into a form

$$\mathbf{y} = \mathbf{\Phi}\mathbf{h} + \boldsymbol{\omega}, \quad (23)$$

where $\mathbf{y}$, $\mathbf{h}$ and $\boldsymbol{\omega}$ are vector representations of $\{(r_{\mathrm{lng}}^{[0]}[n] + r_{\mathrm{lng}}^{[1]}[n])/2\}$, $\{h'_{\mathrm{avg},l}\}$ and $\{\frac{1}{2}\sum_{b=0}^{1} I^{[b]}[n] + \tilde{w}_{\mathrm{lng}}^{[b]}[n]\}$, respectively, and $\mathbf{\Phi}$ is a Toeplitz matrix constructed from $s_{\mathrm{lng}}[n]$. On the basis of (23), we apply the iterative FV-SBL algorithm derived in Appendix A for estimating $h'_{\mathrm{avg},l}$. To initialize FV-SBL, we set the initially estimated value of $h'_{\mathrm{avg},l}$ to zero and obtain the initial noise variance estimate by measuring the power of the non-information bearing observations.

Given the fact that $h'_{\mathrm{avg},l}$ is a cyclic shift of the true CIR with only L_{ch} non-zero taps, the obtained estimates $\{\hat{h}'_{\mathrm{avg},l}\}_{l=0,\ldots,K-1}$ are further used to compute the timing metric for refining the coarse STO estimate. Namely, we circularly shift the CIR estimate by δ and calculate a timing-metric by summarizing the first L_{cp} taps

$$\Lambda_{\epsilon_{\mathrm{f}}}(\delta) = \sum_{l=0}^{L_{\mathrm{cp}}-1} |\hat{h}'_{\mathrm{avg},\langle l+\delta\rangle_K}|^2. \quad (24)$$

Here, we use L_{cp} instead of L_{ch} because the latter is unknown to the receiver. Instead of directly taking the maximum point of $\Lambda_{\epsilon_{\mathrm{f}}}(\delta)$ as the fine STO estimate, we determine it by taking the middle point of the left- and right-most point that can attain the $95\,\%$ maximum of $\Lambda_{\epsilon_{\mathrm{f}}}(\delta)$.

B. UW-Based Channel Estimation and RFO Compensation

Under a highly time-selective vehicular communication channel, the initial preamble-based CIR estimate can become outdated after receiving multiple GFDM symbols. From our packet design, each GFDM symbol is embedded with a UW signal $s_{\mathrm{uw}}[n]$ known by the receiver and therefore can be used for channel tracking. Additionally, it can be used to compensate the RFO, avoiding dedicated pilot subcarriers. For simplicity, the following algorithm derivation assumes perfect STO synchronization. This can be interpreted as that the receiver uses the estimated STO as the true one and any mismatch due to inaccurate STO estimation in practice is counted as additional Gaussian noise.

Fig. 3 shows that between two successive GFDM symbols there is a segment of length $L_{\mathrm{tl}} + L_{\mathrm{hd}}$ that is known by the receiver, i.e., $s_{\mathrm{uw}}[\langle n-L_{\mathrm{tl}}\rangle_N]$ for $n = 0, \ldots, L_{\mathrm{hd}}+L_{\mathrm{tl}}-1$. The distance between two adjacent segments is N. Ignoring the CIR variation during the transmission of the $L_{\mathrm{hd}}+L_{\mathrm{tl}}+N$ samples, the observed two segments at the receiver except the first $L_{\mathrm{cp}}-1$ samples can then be expressed as

$$r_{\mathrm{uw}}^{[b]}[n] = e^{j2\pi\frac{\Omega_{\mathrm{f}}(n+bN)+\theta}{K}} \sum_{l=0}^{L_{\mathrm{ch}}-1} h_l\, s_{\mathrm{uw}}[\langle n-L_{\mathrm{tl}}-l\rangle_N] + \tilde{w}_{\mathrm{uw}}^{[b]}[n] \quad (25)$$

for $n = L_{\mathrm{cp}}-1, \ldots, L_{\mathrm{tl}}+L_{\mathrm{hd}}-1$ and with the segment index $b \in \{0, 1\}$. In (25), the common phase offset θ equals Ω_{f} times the index of the first observed sample of the former segment ($b = 0$) in the complete received sequence $r[n]$, and $\tilde{w}_{\mathrm{uw}}^{[b]}[n]$ represents the effective noise involving interference arising from inaccurate STO estimation and the CIR variation during the transmission of the $L_{\mathrm{hd}}+L_{\mathrm{tl}}+N$ samples.

In a noise-free case, we notice from (25) that

$$r_{\mathrm{uw}}^{[b=0]}[n] \exp\left(j2\pi\frac{\Omega_{\mathrm{f}}N}{K}\right) = r_{\mathrm{uw}}^{[b=1]}[n] \quad (26)$$

for $n = L_{\mathrm{cp}}-1, \ldots, L_{\mathrm{tl}}+L_{\mathrm{hd}}-1$. Under this identification, we can estimate the RFO Ω_{f} by computing the correlation between $r_{\mathrm{uw}}^{[0]}[n]$ and $r_{\mathrm{uw}}^{[1]}[n]$

$$\hat{\Omega}_{\mathrm{f}} = \frac{K}{N(2\pi)}\arg\left[\sum_{n=L_{\mathrm{cp}}-1}^{L_{\mathrm{tl}}+L_{\mathrm{hd}}-1} \mathrm{conj}\left(r_{\mathrm{uw}}^{[0]}[n]\right) r_{\mathrm{uw}}^{[1]}[n]\right]. \quad (27)$$

In fact, the summation in the equation above can also involve all segments received in the past. This approach is also applicable for tracking time-varying Ω_{f} caused by oscillator drifts or changes of Doppler shifts.

After compensating the RFO, we proceed to channel estimation based on (25). The phase offset θ can be treated as a part of the CIR, as it is common to the transmission of all $L_{\rm hd}+L_{\rm tl}+N$ samples. Analogous to the preamble-based CIR estimation, here we adopt FV-SBL to estimate $\{h_l e^{j2\pi\frac{\theta}{K}}\}$. This requires us to first formalize the discrete-time model (25) into a form identical to (23). In the current case, the observation vector $\mathbf{y}$, the channel vector $\mathbf{h}$ and the matrix $\mathbf{\Phi}$ are constructed from $\{(r^{[0]}_{\rm uw}[n]+r^{[1]}_{\rm uw}[n])/2\}_{n=L_{\rm cp}-1,\ldots,L_{\rm tl}+L_{\rm hd}-1}$, $\{h_l e^{j2\pi\frac{\theta}{K}}\}_{l=0,\ldots,L_{\rm cp}-1}$ and $\{s_{\rm uw}[\langle n-L_{\rm tl}\rangle_N]\}_{n=0,\ldots,L_{\rm tl}+L_{\rm hd}-1}$, respectively. On this basis, we can subsequently apply the iterative FV-SBL algorithm derived in Appendix A for estimating the CIR. It also provides an estimate of the effective noise variance needed for subsequent equalization. Considering the temporal correlation of the channel, the current run of FV-SBL can start from the previously obtained CIR and noise variance estimate.

C. LMMSE Equalization

The goal of coherent equalization is to separate superimposed data streams based on the receive samples and the channel estimate, while treating the data symbols as continuous random variables. The N received samples of each GFDM symbol is the outcome of circularly convolving it with the CIR plus noise, thereby permitting simple frequency domain equalization.

Based on the STO estimate, we define the N-point DFT window for each GFDM symbol. The outcome of DFT is

$$R_{\rm gfdm}[\nu]=S_{\rm gfdm}[\nu]\hat{H}[\nu]+\tilde{W}[\nu], \tag{28}$$

where $S_{\rm gfdm}[\nu]$, $\hat{H}[\nu]$ and $\tilde{W}[\nu]$ are the N-point DFTs of the GFDM symbol, estimated CIR and effective noise that incorporates the synchronization and channel estimation errors. In particular, $S_{\rm gfdm}[\nu]$ is comprised of the information-carrying data symbols and the deterministic UW signal

$$S_{\rm gfdm}[\nu]=S_{\rm uw}[\nu]+\sum_k G[\langle\nu-kM\rangle_N]D_{k,u=\langle\nu\rangle_M}, \tag{29}$$

where $S_{\rm uw}[\nu]$ and $G[\nu]$ respectively denote the N-point DFT of $s_{\rm uw}[n]$ given in (7) and the circular pulse shaping filter $g[n]$ in (3), and the auxiliary variable $D_{k,u}$ is defined as

$$D_{k,u}=\sum_{m=0}^{M-1} d_{k,m}e^{-j2\pi\frac{m\nu}{M}}. \tag{30}$$

As both $\hat{H}[\nu]$ and $S_{\rm uw}[\nu]$ are known by the receiver, we can subtract their product from the frequency domain observation

$$\begin{aligned}\tilde{R}_{\rm gfdm}[\nu]&=R_{\rm gfdm}[\nu]-\hat{H}[\nu]S_{\rm uw}[\nu]\\&=\hat{H}[\nu]\sum_k G[\langle\nu-kM\rangle_N]D_{k,\langle\nu\rangle_M}+\tilde{W}[\nu].\end{aligned} \tag{31}$$

In the sequel, the frequency domain equalization will be based on the input-output relation given in (31).

Firstly, we note the presence of inter-symbol interference (ISI) from all active subsymbols due to (30) and inter-carrier interference (ICI) from subcarriers with $G[\langle\nu-kM\rangle_N]\neq 0$. Due to the ISI and ICI, a straightforward application of

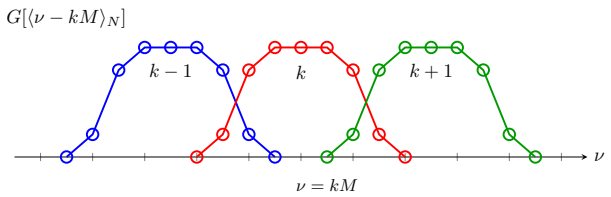

Fig. 4. $G[\langle\nu-kM\rangle_N]$ versus the frequency bin ν for three consecutive subcarriers, where $g(t)$ is constructed from the RC filter with the roll-off factor 0.5 and M equals 5.

LMMSE equalization requires to invert a banded matrix with complexity $O(KM^3)$ [35]. Aiming at an implementation friendly solution, here we present a low complexity approximation. Namely, even though the first subsymbol $\{d_{k,m=0}\}$ is determined by the other subsymbols for the UW generation, we still assume that $\{d_{k,m}\}$ are i.i.d. Gaussian random variables with zero mean and variance equal to the energy $E_{\rm s}$ of each data symbol. Under this assumption, $\{D_{k,u}\}$ as the M-point DFT of $\{d_{k,m}\}$ are also i.i.d. Gaussian random variables but with zero mean and variance $ME_{\rm s}$. By first estimating $\{D_{k,u}\}$ based on (31), we can then generate the approximate LMMSE estimate $\{\hat{d}_{k,m}\}$ by simple M-point IDFT.

Secondly, the LMMSE estimation of $\{D_{k,u}\}$ based on (31) can be split into M groups. This is because for a specific $u\in\{0,1,\ldots,M-1\}$ the information of $\{D_{k,u}\}$ are only contained in $\tilde{R}_{\rm gfdm}[\nu]$ with $\langle\nu\rangle_M=u$, i.e.,

$$\begin{aligned}\tilde{R}_{\rm gfdm}[\kappa M+u]=\hat{H}[\kappa M+u]\sum_k G[\langle(\kappa-k)M+u\rangle_N]D_{k,u}\\+\tilde{W}[\kappa M+u]\quad\kappa=0,1,..,K-1.\end{aligned} \tag{32}$$

Eq. (32) effectively forms a linear system of dimension K. On top of it, we can readily follow [29, Theorem 12.1] to compute the LMMSE estimates $\{\hat{D}_{k,u}\}$ and their estimation error variances $\{\sigma^2_{{\rm D},k,u}\}$. The required complexity depends on the value of u. With the use of the periodic RC filter, there are two possible cases. One is the ICI free case, e.g., for $u=0$ in Fig. 4. In this case, $G[\langle(\kappa-k)M+u\rangle_N]$ is non-zero only if $\kappa=\langle k\rangle_K$. In other words, the system is memoryless, yielding LMMSE estimation complexity $O(K)$. The other is with the presence of ICI, e.g., for $u=2$ in Fig. 4. Then, $G[\langle(\kappa-k)M+u\rangle_N]$ is non-zero for both $\kappa=\langle k\rangle_K$ and $\kappa=\langle k-1\rangle_K$, namely ICI from one neighboring subcarrier. The system becomes non-memoryless and the memory length equals one. Resorting to the Tridiagonal matrix algorithm [36], the LMMSE solution can still be obtained in $O(K)$.

Taking M-point IDFT of $\{\hat{D}_{k,u}\}$, we finally compute the LMMSE estimates of individual data symbols as

$$\hat{d}_{k,m}=\frac{1}{M}\sum_{u=0}^{M-1}\hat{D}_{k,u}e^{j\frac{2\pi um}{M}}, \tag{33}$$

while the error variance of the LMMSE estimate $\hat{D}_{k,u}$ yields

$$\sigma^2_{{\rm d},k,m}=\frac{1}{M^2}\sum_{u=0}^{M-1}\sigma^2_{{\rm D},k,u}. \tag{34}$$

Since the LMMSE equalizer is a biased estimator, we need to compensate the bias before subsequent detection and decoding. The mean and variance in (33) and (34) effectively form an

a-posteriori distribution of $d_{k,m}$, i.e., $\mathcal{CN}(\hat{d}_{k,m}, \sigma^2_{\mathrm{d},k,m})$, by incorporating the likelihood of $d_{k,m}$ given the channel observation and the a-priori distribution of $d_{k,m}$, i.e., $\mathcal{CN}(0, E_\mathrm{s})$. In the context of message passing, e.g., in [37], [38], bias compensation is effectively achieved by a simple divide between the a-posteriori and a-priori distribution

$$\mathcal{CN}(\hat{d}_{\mathrm{ext},k,m}, \sigma^2_{\mathrm{ext},k,m}) \propto \frac{\mathcal{CN}(\hat{d}_{k,m}, \sigma^2_{\mathrm{d},k,m})}{\mathcal{CN}(0, E_\mathrm{s})} \tag{35}$$

with $\frac{\hat{d}_{\mathrm{ext},k,m}}{\sigma^2_{\mathrm{ext},k,m}} = \frac{\hat{d}_{k,m}}{\sigma^2_{\mathrm{d},k,m}}$ and $\sigma^{-2}_{\mathrm{ext},k,m} = \sigma^{-2}_{\mathrm{d},k,m} - E_\mathrm{s}^{-1}$. This is in line with the concept of extrinsic information in the context of iterative decoding, where division in the probability domain is equivalent to subtraction in the log-probability domain.

D. Soft Detection and Decoding

As the final decoder only accepts a sequence of bits plus reliability information, i.e., in terms of log-likelihood ratios (LLRs), we need a soft detector that maps the outcome of the equalizer onto a sequence of LLRs. Briefly, it treats $\hat{d}_{\mathrm{ext},k,m}$ as the observation of $d_{k,m}$ that is attained at the output of an AWGN channel with noise variance $\sigma^2_{\mathrm{ext},k,m}$. Following [39], the bit-wise LLRs are generated and then fed into the channel decoder. As ITS-G5 adopts a convolutional code, channel decoding can be realized by a Viterbi decoder.

E. Complexity Analysis

On the algorithm level, this section presents a complexity analysis, focusing on the most computational intensive receiver algorithms that are GFDM-specific. Compared to mobile handsets powered by a small battery, vehicles can support much more powerful processing capability under a relaxed energy consumption and area constraint [40]. On contrary, the processing time is critical to support latency sensitive applications. Therefore, we consider the level of parallelism in implementation supportable by the proposed algorithms is more important than the number of arithmetic operations.

1) N-point DFT: DFT is often the module at the transceiver that consumes the majority of the processing time budget. At the transmitter, we need K-point DFT analogous to OFDM. However, to perform frequency domain equalization at the receiver, we need to apply N-point DFT for both the N received samples per GFDM symbol and the estimated CIR. According to our configuration in Table II, N equal to 320 is 5 times greater than the 64-point DFT required for OFDM in ITS-G5. In the following, we present two possible solutions.

First, we can use a dedicatedly designed 320-point DFT module. According to Table 3-1 in [41], such module, involving radix-2 and -5 operations, is expected to require about 10^3 latency cycles, equal to $4\,\mu$s at the clock rate of 250 MHz. If we plan to finish the processing of one GFDM symbol before the next one arrives, DFT consumes $12.5\,\%$ of the time budget. This is actually identical to the OFDM case, namely the time spent for 64-point DFT approximately equals $12.5\,\%$ of OFDM symbol duration plus CP.

Second, we can reuse the 64-point DFT plus a 5-point DFT (i.e., one radix-5 operation) for executing 320-point DFT, see Appendix B. By means of parallel processing, this approach allows to realize one 320-point DFT with the latency equal to that of a single 64-point DFT plus a small increment.

Here we also note that the estimated CIR has maximally $L_\mathrm{cp} = 16$ non-zero values, permitting much simpler and faster 320-point DFT operation. Based on the factorization $N = 320 = 20 \times 16$, the approach in Appendix B implies that we need to perform 20-point DFT followed by 16-point DFT. Since the 20-point DFT is applied for a single non-zero value plus 19 zeros, the outcome is straightforward. Then, the effective complexity required for 320-point DFT of the estimated CIR reduces to that of 16-point DFT.

2) LMMSE Equalization: According to Section IV-C, the LMMSE equalization of a GFDM symbol can be split into M independent tasks, where each task can be simultaneously executed. The latency of each task depends on the choice of the pulse shaping filter $g[n]$. If $g[n]$ is chosen to be ICI free, e.g., RC filter with a zero roll-off factor, the latency is identical to perform LMMSE equalization of an OFDM symbol. Otherwise, it depends on the implementation of the Thomas algorithm. Nevertheless, the complexity of both cases scales linearly with the number of data subcarriers. After finishing the $M = 5$ tasks, we need to additionally perform a series of M-point IDFT, depending on the number of data subcarriers. With sufficient computational resources, they all can be conducted in parallel to achieve the minimum latency. In the ideal case, the processing time difference between equalizing a GFDM and OFDM symbol can be marginal, even though the former carries over four times more data symbols.

Concluding from the above algorithmic level analysis, we observe the potential of achieving a low-latency GFDM receiver design. For further quantitative analysis, we shall resort to hardware implementation which will be a part of our future works.

V. Performance Evaluation

In this section, we evaluate the performance of the proposed GFDM-based PHY under two representative ITS-G5 channel models [42] for single-user scenarios, see Table IV and V. All delay taps are modeled as Rayleigh distributed random variables except the first path in the line-of-sight (LOS) case follows a Rice distribution with the K-factor equal to 10. The total channel gain is normalized to one. We assume successful detection of packet arrival, but without knowing the starting point. The CFO is set to the largest possible value under the oscillator precision tolerance specified in [1], i.e., 40 ppm. The configuration of OFDM and GFDM follows Table I and II, respectively. The MCS $1/2$-rate QPSK and $3/4$-rate 64 QAM are of primary concern. The former is the default choice for transmission over CCH and also has been identified as the optimal choice for vehicular safety communication [43]. The latter is the highest oder MCS considered in ITS-G5.

A. Perfect Synchronization and Channel Estimation

Fig. 5-(a) depicts the transmit PSDs of OFDM and GFDM. Under the assumption of perfect synchronization and channel estimation, Fig. 5-(b) shows their PERs attained at different

TABLE IV
URBAN APPROACH LINE-OF-SIGHT (LOS), 119 KM/H DIFFERENTIAL SPEED

	Tap 1	Tap 2	Tap 3	Tap 4
Delay [ns]	0	117	183	333
Power [dB]	0	-8	-10	-15
Doppler [Hz]	0	236	-157	492

TABLE V
HIGHWAY NON-LOS (NLOS), 252 KM/H DIFFERENTIAL SPEED

	Tap 1	Tap 2	Tap 3	Tap 4
Delay [ns]	0	200	433	700
Power [dB]	0	-2	-5	-7
Doppler [Hz]	0	689	-492	886

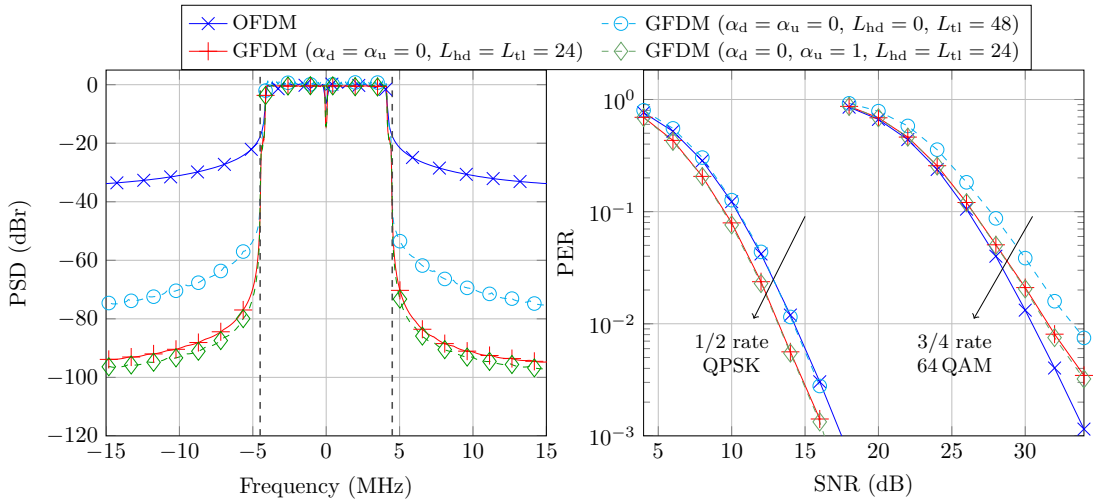

(a) Power spectral density (PSD)

(b) PER under Highway NLOS

Fig. 5. Transmit power spectral density (PSD) and packet error rate (PER) of OFDM and GFDM, where the packet size equals 800 bytes.

signal-to-noise ratios (SNRs), where the SNR measure is defined as E_s/N_0 in [dB].

Three UW designs combined with the GFDM configuration given in Table II are examined. Specifically, the parameters α_d and α_u are the roll-off factors of the periodic RC filters that are respectively used for filtering the data symbols and generating the UW signal. With $\alpha_d = \alpha_u = 0$, GFDM reduces to DFT-s-OFDM, whose spreading factor and DFT size respectively equal M and N. The UW designs for DFT-s-OFDM in the literature always have a fixed tail, i.e., $L_{hd} = 0$ and $L_{tl} = 48$. Our proposal is $L_{hd} = L_{tl} = 24$, yielding lower OOB emission and PERs, see Fig. 5. Furthermore, as a generalization of DFT-s-OFDM, GFDM permits the use of periodic RC filters with arbitrary roll-off factors. For data transmission, the choice $\alpha_d = 0$ ensures ICI-free, easing the implementation of LMMSE equalization. For generating the UW signal, $\alpha_u = 1$ on the other hand can further reduce the OOB emission, see Fig. 5-(a). Since the deterministic UW signal can be easily canceled out at the receiver, a non-zero roll-off factor will not introduce interference to data transmission. Overall, the UW design with $\alpha_d = 0$, $\alpha_u = 1$ and $L_{hd} = L_{tl} = 24$ outperforms the others. Therefore, hereafter it is the default choice for GFDM.

Comparing GFDM with OFDM, Fig. 5-(a) confirms the fulfillment of the standard requirement that the transmit PSD has 0 dBr[8] bandwidth not exceeding 9 MHz [1], [17]. Beyond the 9 MHz bandwidth, the OOB emission shall be as low as possible such that the interference to systems operating in neighboring spectrum outside of the 5.9 GHz frequency band[9] – such as the CEN DSRC system in Europe [17] at 5.8 GHz – can become harmless. It is also a desirable feature for adjacent channels inside the 5.9 GHz frequency band when multiple ITS-G5 radios operate at adjacent channels, i.e., MCO in either single or dual-radio transceiver modes. In Fig. 5-(a), the frequencies of ± 10 MHz effectively correspond to the adjacent channel center frequencies in the considered spectrum. With identical transmit power, the interference caused by OFDM can be up to 60 dB higher than that of GFDM. This indicates that by GFDM with its well-shaped PSD the regulatory requirements in terms of transmit spectrum masks could be sharpened, and thereby the system performance improved.

Fig. 5-(b) shows that GFDM achieves slightly smaller PER than OFDM with $1/2$-rate QPSK. A performance loss appears when switching to the higher order MCS $3/4$-rate 64 QAM. This implies that GFDM relies on the code diversity to combat the self-generated interference and the negative impact introduced by UW embedding. The ensuing part further compares the PERs of GFDM and OFDM when synchronization and channel estimation errors are taken into account.

B. Imperfect Synchronization and Channel Estimation

Without any prior knowledge of the synchronization parameters and the CIR, the synchronization and channel estimation algorithms developed in Sec. IV are needed. They are DA approaches based on the preamble and the UW

[8]Decibels relative to the signal level at the band center.

[9]For ITS-G5 outside of 5,855 MHz to 5,925 MHz.

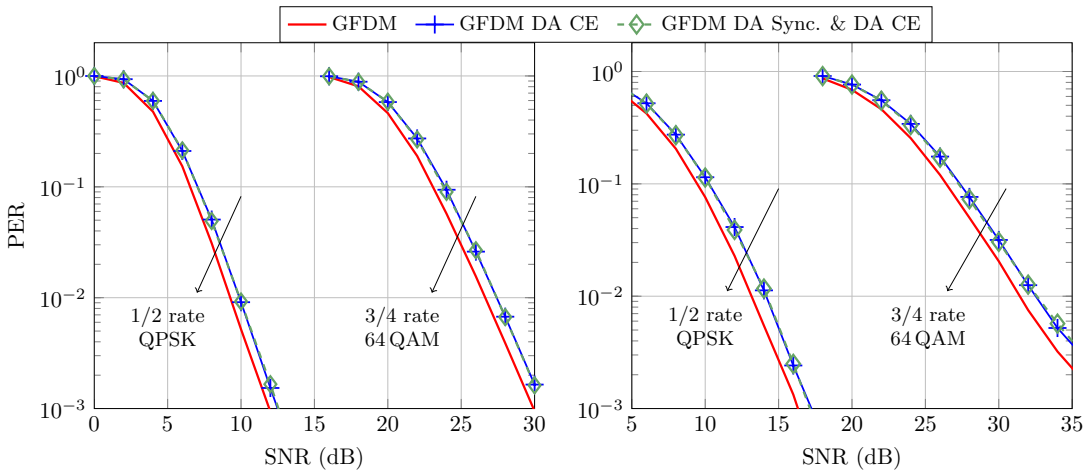

(a) Urban LOS (b) Highway NLOS

Fig. 6. Packet error rate (PER) achieved by GFDM under two channel models, where the packet size equals 800 bytes. Note: unless stated otherwise in the labels the synchronization parameters and the channel coefficients are assumed to be perfectly known by the receiver.

signal. Comparing with the case of perfect synchronization and channel estimation (i.e., curves with label "GFDM"), Fig. 6 shows that the performance loss is mainly due to inaccurate channel knowledge and GFDM is insensitive to the residual synchronization errors. Therefore, in the following comparison with OFDM, the capability of combating time and frequency selective fading channels is the focus.

In order to track the time-varying channel, we let OFDM work with three different channel estimation approaches. First, a midamble [9] identical to the long training sequence in the preamble is periodically inserted into the sequence of OFDM data symbols. In the simulation, every 8 OFDM symbols a midamble is inserted, being labeled as $T_{\mathrm{p}} = 8$. Using the midamble, we perform two types of DA channel estimation by means of FV-SBL. One uses the currently received midamble to predict the channel for coherently detecting subsequent OFDM data symbols until the next midamble is received. The other one takes the average on the observation of two consecutive midambles and estimate the channel for coherent detection of the OFDM data symbols in between. The former does not need to wait for receiving two midambles, while the latter provides more accurate channel estimates.

Instead of inserting midambles, the third approach considered here is a DD approach. ITS-G5 uses convolutional code and bit-interleaving is only among bits carried by the same OFDM symbol. Given the Markov property of convolutional code, we can decode the first OFDM symbol before receiving the second one. By reproducing the first OFDM symbol at the output of the decoder, we further use it as an auxiliary midamble to predict the channel for the next OFDM data symbol. This approach does not waste time resources for inserting dedicated midambles. However, the processing complexity and latency are both higher than the above two DA approaches. They can become unacceptable if other channel codes for achieving more stringent reliability requirement are adopted, e.g., turbo or low density parity check codes. Alternatively, it is possible to directly make hard-decision on the data symbol estimates attained by the equalizer without exploiting the error correction capability at the decoder. However, the resulting high symbol error rate can lead to a high PER error floor, being problematical for ultra-reliable communication as well. Therefore, it is not considered here.

For GFDM, we save the use of CPs for embedding training samples into each GFDM data symbol via the UW signal. By doing so, we are able to perform simple DA channel estimation without requiring extra time resources.

Fig. 7 shows that for OFDM the DD approach generally outperforms both DA approaches. The midamble period T_{p} of 8 OFDM symbols becomes inefficient to handle fast changing channels at the high-order MCS. GFDM DA can achieve up to $50\,\%$ reduction on the PER of OFDM DD under the challenging highway channel model.

C. PHY-Level Throughput

Table III lists the achievable data rates of 8 MCSs without considering the preamble overhead and the dropped packets due to decoding errors. This subsection evaluates the PHY-level throughputs of OFDM and GFDM according to

$$\mathrm{Thr}_{\mathrm{gfdm}} = \frac{8N_{\mathrm{pl}}(1-\mathrm{PER}_{\mathrm{gfdm}})}{(32N_{\mathrm{gfdm}}+40+6.3+6.4)\cdot 10^{-6}} \tag{36}$$

$$\mathrm{Thr}_{\mathrm{ofdm}} = \frac{8N_{\mathrm{pl}}(1-\mathrm{PER}_{\mathrm{ofdm}})}{(8N_{\mathrm{ofdm}}+40)\cdot 10^{-6}}. \tag{37}$$

In words, the number $8N_{\mathrm{pl}}$ of bits per packet divides the packet duration and then multiplies the rate $(1-\mathrm{PER})$ of a packet being successfully received. Specifically, the duration of one GFDM packet involves overhead from the insertion of preamble, the $6.3\,\mu$s prefix of the first GFDM data symbol and $6.4\,\mu$s suffix of the last GFDM data symbol to ensure low OOB emission. Additionally, the last GFDM symbol effectively carries the final information bits with the number equal to the remainder after the division of $(8N_{\mathrm{pl}}+22)$ by N_{bpgfdm}, see (8). It may happen that only very few information bits are carried by the last GFDM symbol, which still lasts $32\,\mu$s. On contrary, OFDM handles such remaining bits more

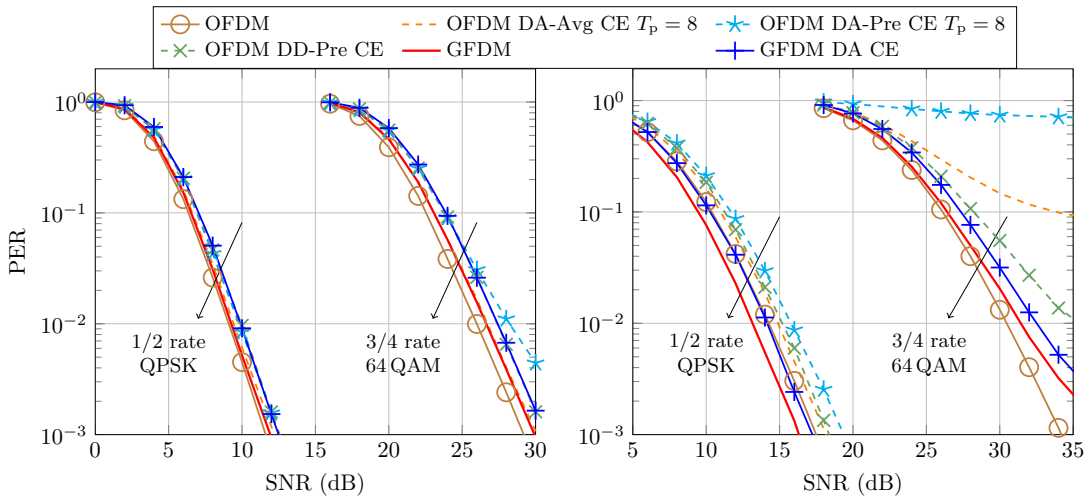

(a) Urban LOS (b) Highway NLOS

Fig. 7. Packet error rate (PER) achieved by GFDM and OFDM under two channel models, where the packet size equals 800 bytes. Note: unless stated otherwise in the labels the synchronization parameters and the channel coefficients are assumed to be perfectly known by the receiver.

efficiently, as one OFDM symbol only takes $8\,\mu$s. However, the $25\,\%$ CP overhead applies for each OFDM symbol. From Table III, each OFDM symbol is less efficient than GFDM in conveying information bits. Comparing the overhead of GFDM and OFDM, the former does not increase with the packet size and the latter does. Based on the following relation on the number of GFDM and OFDM symbols to deliver the same packet size

$$N_{\text{gfdm}} \leq \left\lceil \frac{N_{\text{ofdm}}}{(13/3)} \right\rceil \leq \frac{N_{\text{ofdm}}}{(13/3)} + 1, \tag{38}$$

we can derive that one GFDM packet is guaranteed to be shorter than one OFDM packet if $N_{\text{ofdm}} \geq 73$.

Fig. 8 depicts the throughputs of the default MCS scheme attained at different packet sizes. In principle, two conflicting effects can affect the throughput. One is from the preamble overhead, reducing as the packet size increases. The other is the probability of encountering error bits, i.e., PER. It increases when we have more bits to decode. As PER reduces to zero as the SNR increases, the benefit of having a larger packet size appears only if the SNR is large enough. For instance, at 15 dB, the gain of GFDM over OFDM is mainly due to its shorter packet length. It is expected to increase with the packet size. As the SNR decreases, the PER plays a more critical role on the throughput. The preserved and even enlarged gains at 10 dB and 5 dB indicate that GFDM achieves lower PERs, being more reliable than OFDM at low SNRs.

Fig. 9 depicts the throughputs achieved by all MCS schemes indicated in Table III. They are evaluated at a small and moderate packet size, namely, 400 and 800 bytes. The observations are generally aligned with those obtained from Fig. 8 at the default MCS, i.e., MCS with index 2. Particularly, Fig. 9-(a) and (d) indicate that it is beneficial to use GFDM at difficult channel conditions. In Fig. 9-(c), one exception is that OFDM slightly outperforms GFDM at the MCS with index 4, 7 and 8. These indices correspond to the three highest order MCSs, requiring the three smallest numbers of OFDM data symbols

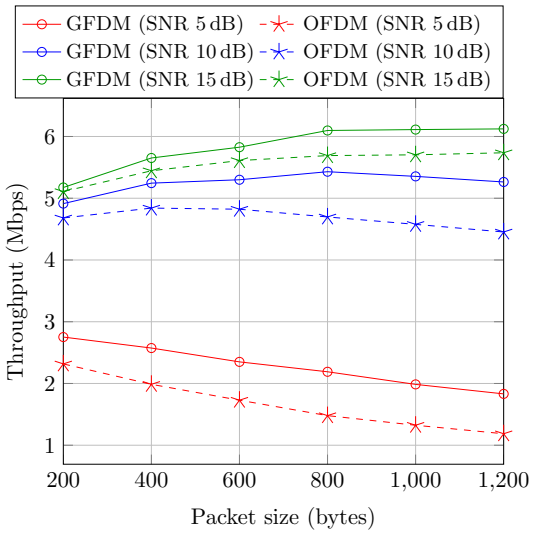

Fig. 8. PHY-level throughput of GFDM (DA CE) and OFDM (DD-Pre CE) under the highway NLOS channel for different SNR values in [dB].

to carry the 400 bytes, i.e., $N_{\text{ofdm}} < 73$. In this case, the GFDM packet may still take longer transmission time than OFDM. However, the gain reduces and even disappears, when the packet size is doubled, see Fig. 9-(f).

VI. Conclusion

Considering the specifications and requirements defined in ITS-G5, this paper has presented a GFDM-based PHY design for vehicular communication. On the transmitter side, we have designed the GFDM symbol to achieve three goals: *(i)* embed training sequences for channel tracking, *(ii)* avoid dedicated CPs for temporal efficiency, and *(iii)* ensure low OOB emission to adjacent channels or frequency bands for spectral efficiency. On the receiver side, we have aimed at synchronization, channel estimation and equalization. In particular, we have developed a low complexity variant of variational SBL for assisting fine STO synchronization and

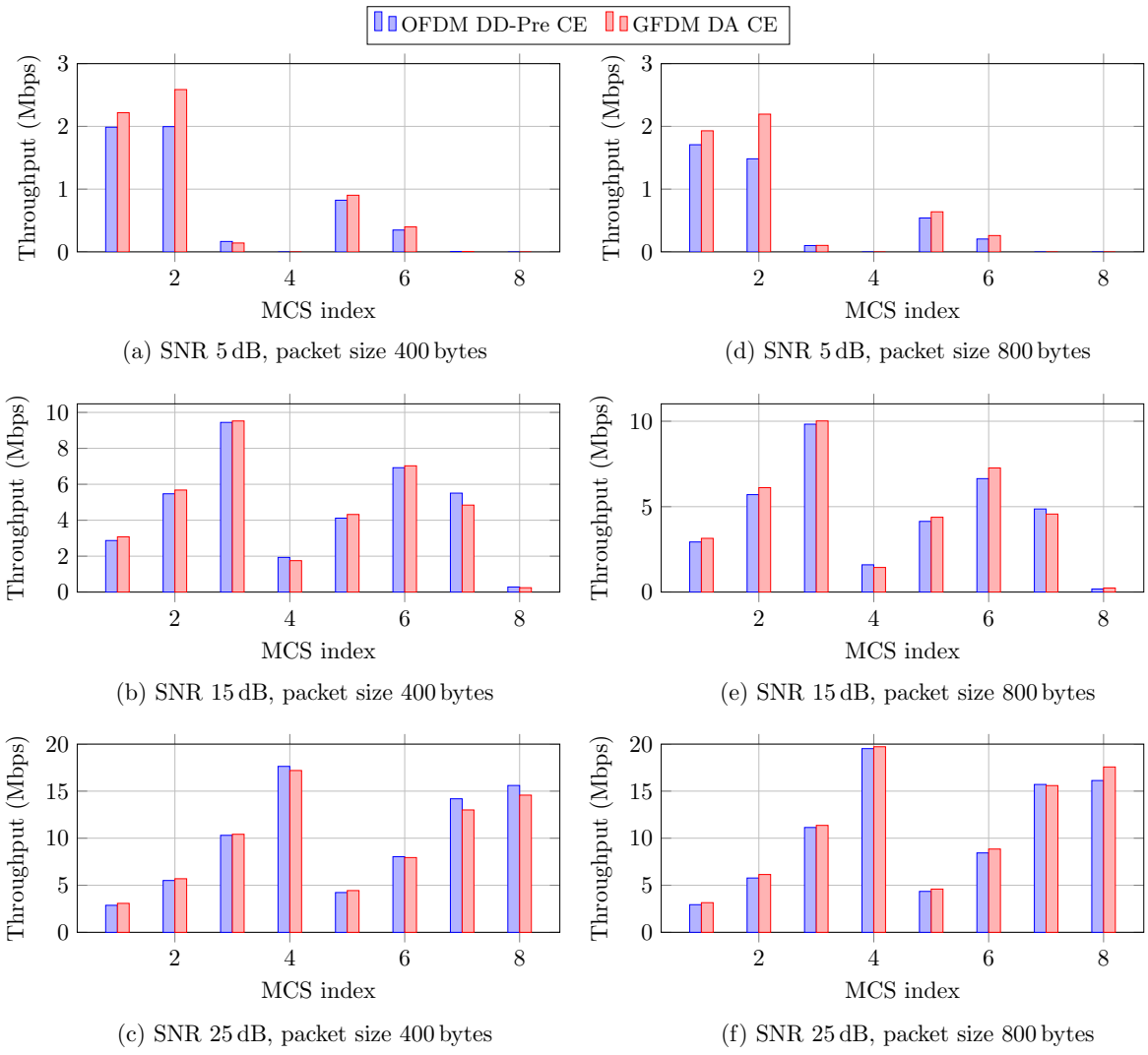

(a) SNR 5 dB, packet size 400 bytes

(d) SNR 5 dB, packet size 800 bytes

(b) SNR 15 dB, packet size 400 bytes

(e) SNR 15 dB, packet size 800 bytes

(c) SNR 25 dB, packet size 400 bytes

(f) SNR 25 dB, packet size 800 bytes

Fig. 9. PHY-level throughput of GFDM and OFDM under the Highway NLOS channel model and for different MCSs.

estimating the sparse CIR. For tackling the interference introduced by the channel and the waveform GFDM itself, we have followed the LMMSE criterion and aimed at an approximation whose implementation complexity can be comparable to that of OFDM.

Benefiting from its higher temporal and spectral efficiency, the GFDM-based PHY can achieve up to 60 dB less ACI, 50 % lower PER and two times higher PHY-level throughput than the standard-compliant OFDM-based solution. The achieved gain is particularly pronounced in challenging conditions, e.g., low SNRs, high mobility and high-order MCS. Compared to the OFDM-based state-of-the-art solutions ITS-G5 and LTE-V2X, the waveform GFDM enables a performance gain at upper protocol layers and can eventually improve road safety and traffic efficiency of ITS. The advantage will amplify when the system simultaneously operates over multiple channels of the 5.9 GHz frequency band.

ACKNOWLEDGEMENTS

This work was supported by the German Science Foundation (DFG) within the priority program "Cooperative Interacting Cars (CoInCar)" (SPP 1835).

APPENDIX A
VARIATIONAL SPARSE BAYESIAN LEARNING (SBL)

Consider the following linear model

$$\mathbf{y} = \mathbf{\Phi}\mathbf{h} + \boldsymbol{\omega}, \tag{A.1}$$

where $\mathbf{y} \in \mathbb{C}^{N_\circ}$ is the observation vector, $\mathbf{\Phi} \in \mathbb{C}^{N_\circ \times L}$ is a design matrix with L columns, i.e., $\{\boldsymbol{\phi}_l\}$, the vector $\mathbf{h} = [h_1, h_2, \ldots, h_L]^T$ collects the coefficients to be estimated, and $\boldsymbol{\omega} \in \mathbb{C}^{N_\circ}$ represents the additive Gaussian noise with zero mean and variance τ^{-1}. In the context of SBL, an estimate of $\mathbf{h}$ with only a few non-zero coefficients is encouraged to be selected for reconstructing the observation vector $\mathbf{y}$. This is achieved by constraining each coefficient h_l with a parametric prior $p(h_l|\alpha_l)$, which is symmetric with respect to zero and the sparsity parameter α_l shall be inversely proportional to the width of the probability density function (pdf) $p(h_l|\alpha_l)$, e.g., a Gaussian distribution $p(h_l|\alpha_l) \propto \exp(-\alpha_l|h_l|^2)$. For compactly denoting $\{\alpha_l\}$, we introduce the vector $\boldsymbol{\alpha}$.

In the literature, one important class of algorithms to solve the above SBL problem is based on the variational approximation for Bayesian interference, e.g., [44]–[46]. To

avoid the matrix inversion required by them, here we derive a low complexity variant of variational SBL by using a fully factorized variational proxy pdf, namely, FV-SBL.

Specifically, we factorize the target distribution $p(\mathbf{h}, \boldsymbol{\alpha}, \tau|\mathbf{y})$ as

$$\begin{aligned} p(\mathbf{h}, \boldsymbol{\alpha}, \tau|\mathbf{y}) &\propto p(\mathbf{y}|\mathbf{h}, \tau)p(\tau)\prod_l p(h_l|\alpha_l)p(\alpha_l) \\ &\propto e^{-\tau\|\mathbf{y}-\boldsymbol{\Phi}\mathbf{h}\|^2}p(\tau)\prod_l p(h_l|\alpha_l)p(\alpha_l) \end{aligned} \quad \text{(A.2)}$$

where the prior pdf $p(\alpha_l)$ and $p(\tau)$ are selected to be Gamma distributions

$$p(\alpha_l) = \mathrm{Ga}(\alpha_l|a_l, b_l), \qquad p(\tau) = \mathrm{Ga}(\tau|c, d). \quad \text{(A.3)}$$

Here, we choose $a_l = b_l = c = d = 0$ for obtaining non-informative prior pdfs. Our aim is to approximate the target distribution by an alternative pdf $q(\mathbf{h}, \boldsymbol{\alpha}, \tau) = q(\tau)\prod_l q(h_l)q(\alpha_l)$, namely

$$\hat{q}(\mathbf{h}, \boldsymbol{\alpha}, \tau) = \arg\min \mathrm{KL}\left[q(\mathbf{h}, \boldsymbol{\alpha}, \tau)||p(\mathbf{h}, \boldsymbol{\alpha}, \tau|\mathbf{y})\right], \quad \text{(A.4)}$$

where $\mathrm{KL}(\cdot||\cdot)$ represents the Kullback-Leibler divergence between two pdfs. Due to fully factorization of $q(\mathbf{h}, \boldsymbol{\alpha}, \tau)$, the $L \times L$ matrix inversion needed in [44], [46] can be avoided. Unlike [45], we avoid to introduce a set of admissible hidden data vectors for deriving a tractable problem solver.

Since the objective function is convex with respect to individual pdfs, we can locally minimize it with respect to one pdf while fixing the others. By successively and iteratively refining the pdfs, the convergence to a local minimum is guaranteed, but the global optimality depends on the starting point of the iterative process. Skipping detailed derivations, the update equations for the pdfs are given as

$$\begin{aligned} q(h_l) &\propto \exp\left(-(\hat{\tau}\|\boldsymbol{\phi}_l\|^2 + \hat{\alpha}_l)\left|h_l - \frac{\hat{\tau}\boldsymbol{\phi}_l^H(\mathbf{y} - \boldsymbol{\Phi}_{\setminus l}\hat{\mathbf{h}}_{\setminus l})}{\hat{\tau}\|\boldsymbol{\phi}_l\|^2 + \hat{\alpha}_l}\right|^2\right) \\ q(\alpha_l) &\propto \mathrm{Ga}\left(\alpha_l\middle|1, |\hat{h}_l|^2 + \sigma_{\mathrm{h},l}^2\right) \\ q(\tau) &\propto \mathrm{Ga}\left(\tau\middle|N_\mathrm{o}, \|\mathbf{y} - \boldsymbol{\Phi}\hat{\mathbf{h}}\|^2 + \sum_l \sigma_{\mathrm{h},l}^2\|\boldsymbol{\phi}_l\|^2\right), \end{aligned} \quad \text{(A.5)}$$

where $\hat{h}_l$, $\hat{\tau}$ and $\hat{\alpha}_l$ stand for the mean value of h_l, τ and α_l given their pdfs $q(h_l)$, $q(\tau)$ and $q(\alpha_l)$, respectively. The variance of h_l is denoted as $\sigma_{\mathrm{h},l}^2$. The matrix $\boldsymbol{\Phi}_{\setminus l}$ is obtained by deleting the lth column of $\boldsymbol{\Phi}$, while the vector $\hat{\mathbf{h}}_{\setminus l}$ contains all $\{\hat{h}_{l'}\}$ except $l' = l$. From (A.5), we can notice the pdfs are fully parameterizable by $\{\hat{h}_l, \sigma_{\mathrm{h},l}^2, \hat{\alpha}_l\}$ and $\hat{\tau}$. Therefore, iteratively updating pdfs boils down to iteratively searching for $\{\hat{h}_l, \sigma_{\mathrm{h},l}^2, \hat{\alpha}_l\}$ and $\hat{\tau}$.

Analogous to [46], we can repeatedly update $q(h_l)$ and $q(\alpha_l)$ for a given l, while the other pdfs are fixed. This leads to a sequence of updates on $\hat{\alpha}_l$, converging to

$$\hat{\alpha}_l^{[\infty]} = \frac{\hat{\tau}^2\|\boldsymbol{\phi}_l\|^4}{|\hat{\tau}\boldsymbol{\phi}_l^H(\mathbf{y} - \boldsymbol{\Phi}_{\setminus l}\hat{\mathbf{h}}_{\setminus l})|^2 - \hat{\tau}^2\|\boldsymbol{\phi}_l\|^2} \quad \text{(A.6)}$$

if $|\hat{\tau}\boldsymbol{\phi}_l^H(\mathbf{y} - \boldsymbol{\Phi}_{\setminus l}\hat{\mathbf{h}}_{\setminus l})|^2 > \hat{\tau}^2\|\boldsymbol{\phi}_l\|^2$; otherwise, $\hat{\alpha}_l^{[\infty]} = \infty$. Using the identified stationary points of $\{\hat{\alpha}_l\}$, we are able to speed up the convergence of the iterative solution.

Algorithm 1 FV-SBL

Initialize $\hat{\tau}$ and $\{\hat{h}_l\}$
In the context of this paper, $N_\mathrm{iter} \leftarrow 12$
while $N_\mathrm{iter} \neq 0$ **do**
  for $l = 1$ to L **do**
    if $|\hat{\tau}\boldsymbol{\phi}_l^H(\mathbf{y} - \boldsymbol{\Phi}_{\setminus l}\hat{\mathbf{h}}_{\setminus l})|^2 > \hat{\tau}^2\|\boldsymbol{\phi}_l\|^2$ **then**
      $\hat{\alpha}_l \leftarrow \frac{\hat{\tau}^2\|\boldsymbol{\phi}_l\|^4}{|\hat{\tau}\boldsymbol{\phi}_l^H(\mathbf{y} - \boldsymbol{\Phi}_{\setminus l}\hat{\mathbf{h}}_{\setminus l})|^2 - \hat{\tau}^2\|\boldsymbol{\phi}_l\|^2}$
    else
      $\hat{\alpha}_l \leftarrow 10^8$
    end if
    $\hat{h}_l \leftarrow \frac{\hat{\tau}\boldsymbol{\phi}_l^H(\mathbf{y} - \boldsymbol{\Phi}_{\setminus l}\hat{\mathbf{h}}_{\setminus l})}{\hat{\tau}\|\boldsymbol{\phi}_l\|^2 + \hat{\alpha}_l}$
    $\sigma_{\mathrm{h},l}^2 \leftarrow (\hat{\tau}\|\boldsymbol{\phi}_l\|^2 + \hat{\alpha}_l)^{-1}$
  end for
  $\hat{\tau} \leftarrow \frac{N_\mathrm{o}}{\|\mathbf{y} - \boldsymbol{\Phi}\hat{\mathbf{h}}\|^2 + \sum_l \sigma_{\mathrm{h},l}^2\|\boldsymbol{\phi}_l\|^2}$
  $N_\mathrm{iter} \leftarrow N_\mathrm{iter} - 1$
end while

Algorithm 1 lists the key steps of the above-derived FV-SBL. Its arithmetic complexity is $O(N_\mathrm{iter}L^2 + N_\mathrm{o}L)$. Since $\boldsymbol{\Phi}$ is typically pre-defined, many values can be computed in advance, e.g., $\boldsymbol{\phi}_l^H\boldsymbol{\Phi}_{\setminus l}$ and $\|\boldsymbol{\phi}_l\|^2$ for $l = 1, \ldots, L$. Additionally, the value $\|\mathbf{y}\|^2$ and $\boldsymbol{\phi}_l^H\mathbf{y}$ for $l = 1, \ldots, L$ are invariant over iterations and therefore only need to be calculated once.

APPENDIX B
(KM)-POINT DFT VIA K- AND M-POINT DFT

Given N samples $y[n]$ with $n = 0, 1, \ldots, N-1$, our goal is to compute its N-point DFT

$$Y[\nu] = \sum_{n=0}^{N-1} y[n]e^{-j2\pi\frac{n\nu}{N}}. \quad \text{(B.1)}$$

Considering the factorization $N = KM$, we proceed to realize the above computations via K- and M-point DFT.

Let us start from variable interchanges, i.e., $\nu \leftarrow \alpha M + \beta$ and $n \leftarrow bK + a$, with $\alpha = 0, 1, \ldots, K-1$, $\beta = 0, 1, \ldots, M-1$, $a = 0, 1, \ldots, K-1$, and $b = 0, 1, \ldots, M-1$

$$\begin{aligned} Y[\alpha M + \beta] = \sum_{a=0}^{K-1}\left\{\left[\sum_{b=0}^{M-1} y[bK + a]e^{-j2\pi\frac{b\beta}{M}}\right]e^{-j2\pi\frac{a\beta}{N}}\right\} \\ \cdot e^{-j2\pi\frac{\alpha a}{K}}. \end{aligned} \quad \text{(B.2)}$$

On the basis of (B.2), we further notice the inner summation in $[\cdot]$ corresponds to M-point DFT. After multiplying with $e^{-j2\pi\frac{a\beta}{N}}$, the outer summation corresponds to K-point DFT. Specifically, by arranging the sequence $y[n]$ of N samples into a $M \times K$ matrix via row-by-row writing, one possible implementation of (B.2) consists of the following steps:

1) Apply M-point DFT on the column basis;
2) Perform element-wise multiplication with $e^{-j2\pi\frac{a\beta}{N}}$, where a and β are the column and row index;
3) Apply K-point DFT on the row basis.

Reading out the matrix column-by-column, we consequently have $\{Y[\nu]\}_{\nu=0,1,\ldots,N-1}$. Exploring the maximum possible parallelism, the latency of the above-three steps equals that of one M-point DFT, one multiplication and one K-point DFT.

REFERENCES

[1] Institute of Electrical and Electronics Engineers (IEEE), *IEEE Standard for Information technology—telecommunications and information exchange between systems Local and metropolitan area networks—specific requirements Part 11: Wireless LAN Medium Access Control (MAC) and Physical Layer (PHY) Specifications, IEEE std. 802.11-2016*, 2016.

[2] A. Festag, "Cooperative intelligent transport systems standards in Europe," *IEEE Commun. Mag.*, vol. 52, no. 12, pp. 166–172, Dec. 2014.

[3] J. Kenney, "Dedicated Short-Range Communications (DSRC) standards in the United States," *Proc. of the IEEE*, vol. 99, no. 7, pp. 1162–1182, Jul. 2011.

[4] R. Blasco, H. Do, S. Shalmashi, S. Sorrentino, and Y. Zang, "3GPP LTE enhancements for V2V and comparison to IEEE 802.11p," in *ITS European Congress*, Glasgow, Scotland, Jun. 2016, pp. 1–10.

[5] G. Acosta-Marum and M. A. Ingram, "Six time- and frequency-selective empirical channel models for vehicular wireless LANs," *IEEE Veh. Technol. Mag.*, vol. 2, no. 4, pp. 4–11, Dec. 2007.

[6] C. F. Mecklenbräuker *et al.*, "Vehicular channel characterization and its implications for wireless system design and performance," *Process. of the IEEE*, vol. 99, no. 7, pp. 1189–1212, Jul. 2011.

[7] Z. Zhao, X. Cheng, M. Wen, B. Jiao, and C. X. Wang, "Channel estimation schemes for IEEE 802.11p standard," *IEEE Intelligent Transportation Syst. Mag.*, vol. 5, no. 4, pp. 38–49, Oct. 2013.

[8] S. I. Kim, H. S. Oh, and H. K. Choi, "Mid-amble aided OFDM performance analysis in high mobility vehicular channel," in *Proc. IEEE Symp. on Intelligent Veh.*, Eindhoven, Netherlands, Jun. 2008, pp. 751–754.

[9] W. Cho, S. I. Kim, H. k. Choi, H. S. Oh, and D. Y. Kwak, "Performance evaluation of V2V/V2I communications: The effect of midamble insertion," in *Proc. IEEE Int. Conf. on Wireless Commun., Veh. Technol., Inf. Theory and Aerospace Electron. Syst. Technol. (Wireless VITAE)*, Aalborg, Denmark, May 2009, pp. 793–797.

[10] C. S. Lin, C. K. Sun, J. C. Lin, and B. C. Chen, "Performance evaluations of channel estimations in IEEE 802.11p environments," in *Proc. IEEE Int. Conf. on Ultra Modern Telecommun. Workshops*, St.Petersburg, Russia, Oct. 2009, pp. 1–5.

[11] C. S. Lin and J. C. Lin, "Novel channel estimation techniques in IEEE 802.11p environments," in *Proc. IEEE Veh. Technol. Conf. (VTC Spring)*, Taipei, Taiwan, May 2010, pp. 1–5.

[12] K. K. Nagalapur, F. Brännström, and E. G. Ström, "On channel estimation for 802.11p in highly time-varying vehicular channels," in *Proc. IEEE Int. Conf. on Commun. (ICC)*, Sydney, Australia, Jun. 2014, pp. 5659–5664.

[13] J. A. Fernandez, K. Borries, L. Cheng, B. V. K. V. Kumar, D. D. Stancil, and F. Bai, "Performance of the 802.11p physical layer in vehicle-to-vehicle environments," *IEEE Trans. Veh. Technol.*, vol. 61, no. 1, pp. 3–14, Jan. 2012.

[14] T. Zemen, L. Bernado, N. Czink, and A. F. Molisch, "Iterative time-variant channel estimation for 802.11p using generalized discrete prolate spheroidal sequences," *IEEE Trans. Veh. Technol.*, vol. 61, no. 3, pp. 1222–1233, Mar. 2012.

[15] C. Campolo and A. Molinaro, "Multichannel communications in vehicular ad hoc networks: a survey," *IEEE Commun. Mag.*, vol. 51, no. 5, pp. 158–169, May 2013.

[16] Institute of Electrical and Electronics Engineers (IEEE), *IEEE standard for wireless access in vehicular environments (WAVE) - Multi-channel operation, IEEE std. 1609.4-2016*, 2016.

[17] *ETSI EN 302 571 V2.0.3 (Draft) ITS; Radiocommunications Equipment Operating in the 5 855 MHz to 5 925 MHz Frequency Band; Harmonised Standard Covering the Essential Requirements of Article 3.2 of Directive 2014/53/EU*, ETSI Std., Mar. 2016.

[18] G. Wunder *et al.*, "5GNOW: Non-orthogonal, asynchronous waveforms for future mobile applications," *IEEE Commun. Mag.*, vol. 52, no. 2, pp. 97–105, Feb. 2014.

[19] X. Zhang, M. Jia, L. Chen, J. Ma, and J. Qiu, "Filtered-OFDM-Enabler for flexible waveform in the 5th generation cellular networks," in *Proc. IEEE Global Telecommun. Conf. (GLOBECOM)*, San Diego, CA, USA, Dec. 2015, pp. 1–6.

[20] T. Wild, F. Schaich, and Y. Chen, "5G air interface design based on universal filtered (UF-)OFDM," in *Proc. IEEE Int. Conf. on Digital Signal Process. (DSP)*, Hong Kong, China, Aug. 2014, pp. 699–704.

[21] M. Bellanger *et al.*, "FBMC physical layer: a primer," PHYDYAS project, Tech. Rep., Jun. 2010. [Online]. Available: http://www.ict-phydyas.org/teamspace/internal-folder/FBMC-Primer_06-2010.pdf

[22] N. Michailow *et al.*, "Generalized frequency division multiplexing for 5th generation cellular networks," *IEEE Trans. Commun.*, vol. 62, no. 9, pp. 3045–3061, Sep. 2014.

[23] H. Lin and P. Siohan, "Multi-carrier modulation analysis and WCP-COQAM proposal," *EURASIP Journal on Advances in Signal Processing*, vol. 2014, no. 1, p. 79, May 2014.

[24] L. Deneire, B. Gyselinckx, and M. Engels, "Training sequence versus cyclic prefix-a new look on single carrier communication," *IEEE Commun. Lett.*, vol. 5, no. 7, pp. 292–294, Jul. 2001.

[25] H. Witschnig, T. Mayer, A. Springer, A. Koppler, L. Maurer, M. Huemer, and R. Weigel, "A different look on cyclic prefix for SC/FDE," in *Proc. IEEE Int. Symp. on Personal, Indoor and Mobile Radio Commun. (PIMRC)*, vol. 2, Lisbon, Portugal, Sep. 2002, pp. 824–828.

[26] M. Huemer, C. Hofbauer, and J. B. Huber, "Unique word prefix in SC/FDE and OFDM: A comparison," in *Proc. IEEE Globecom Workshops*, Miami, USA, Dec. 2010, pp. 1296–1301.

[27] A. Sahin, R. Yang, M. Ghosh, and R. L. Olesen, "An improved unique word DFT-spread OFDM scheme for 5G systems," in *Proc. IEEE Globecom Workshops*, San Diego, USA, Dec. 2015, pp. 1–6.

[28] M. E. Tipping, "Sparse bayesian learning and the relevance vector machine," *J. Mach. Learn. Res.*, vol. 1, pp. 211–244, Sep. 2001.

[29] S. M. Kay, *Fundamentals of Statistical Signal Processing, Volume I: Estimation Theory*. Prentice Hall PTR, 1993.

[30] ETSI, *ITS; Access layer Specification for Intelligent Transport Systems Operating in the 5 GHz Frequency Band (ETSI EN 302 663 V1.2.0)*, Nov. 2012.

[31] M. Danneberg, N. Michailow, I. Gaspar, D. Zhang, and G. Fettweis, "Flexible GFDM implementation in FPGA with support to run-time reconfiguration," in *Proc. IEEE Veh. Technol. Conf. (VTC Fall)*, Boston, USA, Sep. 2015, pp. 1–2.

[32] H. Minn, V. K. Bhargava, and K. B. Letaief, "A robust timing and frequency synchronization for OFDM systems," *IEEE Trans. Wireless Commun.*, vol. 2, no. 4, pp. 822–839, Jul. 2003.

[33] T.-D. Chiueh and P.-Y. Tsai, *OFDM Baseband Receiver Design for Wireless Communications*. Wiley Publishing, 2007.

[34] Y. Mostofi and D. C. Cox, "ICI mitigation for pilot-aided OFDM mobile systems," *IEEE Trans. Wireless Commun.*, vol. 4, no. 2, pp. 765–774, Mar. 2005.

[35] M. Matthé, L. L. Mendes, N. Michailow, D. Zhang, and G. Fettweis, "Widely linear estimation for space-time-coded GFDM in low-latency applications," *IEEE Trans. Commun.*, vol. 63, no. 11, pp. 4501–4509, Nov. 2015.

[36] L. Thomas, "Elliptic problems in linear differential equations over a network," Watson Sci. Comput. Lab Report, Columbia University, Tech. Rep., 1949.

[37] M. Senst and G. Ascheid, "How the framework of expectation propagation yields an iterative IC-LMMSE MIMO receiver," in *Proc. IEEE Global Telecommun. Conf. (GLOBECOM)*, Houston, Texas, USA, Dec. 2011.

[38] D. Zhang, L. L. Mendes, M. Matthé, I. S. Gaspar, N. Michailow, and G. P. Fettweis, "Expectation propagation for near-optimum detection of MIMO-GFDM signals," *IEEE Trans. Wireless Commun.*, vol. 15, no. 2, pp. 1045–1062, Feb. 2016.

[39] G. Caire, G. Taricco, and E. Biglieri, "Bit-interleaved coded modulation," *IEEE Trans. Inf. Theory*, vol. 44, no. 3, pp. 927–946, May 1998.

[40] N. Lu, N. Cheng, N. Zhang, X. Shen, and J. W. Mark, "Connected vehicles: Solutions and challenges," *IEEE J. Internet Things*, vol. 1, no. 4, pp. 289–299, Aug. 2014.

[41] Xilinx, *Discrete Fourier Transform v4.0, LogiCORE IP Product Guide*, Nov. 2015.

[42] ETSI, *Intelligent Transport Systems (ITS); Access Layer; ITS-G5 Channel Models and Performance Analysis Framework (ETSI TS 103 257 V0.0.2)*, Apr. 2017.

[43] D. Jiang, Q. Chen, and L. Delgrossi, "Optimal data rate selection for vehicle safety communications," in *Proc. ACM Int. Workshop on Veh. Internetwork. (VANET)*, San Francisco, USA, Sep. 2008, pp. 30–38.

[44] C. M. Bishop and M. E. Tipping, "Variational relevance vector machines," in *Proc. Conf. on Uncertainty in Artificial Intell. (UAI)*, San Francisco, USA, Jul. 2000, pp. 46–53.

[45] D. Shutin and B. H. Fleury, "Sparse variational bayesian SAGE algorithm with application to the estimation of multipath wireless channels," *IEEE Trans. Signal Process.*, vol. 59, no. 8, pp. 3609–3623, Aug. 2011.

[46] D. Shutin, T. Buchgraber, S. R. Kulkarni, and H. V. Poor, "Fast variational sparse bayesian learning with automatic relevance determination for superimposed signals," *IEEE Trans. Signal Process.*, vol. 59, no. 12, pp. 6257–6261, Dec. 2011.